Monolayer force generation and transmission is dictated by focal adhesion distribution

John Robert Davis[1,2‡*], Josephine Solowiej-Wedderburn[3,4,5‡], Sebastián L. Vega[6,7] Jason A. Burdick[8], Carina Dunlop[3,9*], and Nicolas Tapon[2,9*]

[1] Hungry Tissue Lab, Division of Molecular and Cellular Function, School of Biological Sciences, Faculty of Biology Medicine Health, University of Manchester, Manchester, UK
[2] Apoptosis and Proliferation Control Laboratory, The Francis Crick Institute, London, UK
[3] School of Mathematics and Physics, University of Surrey, Guildford, UK
[4] Department of Mathematics and Mathematical Statistics, Umeå University, Umeå, Sweden
[5] Integrated Science Lab, Umeå University, Umeå, Sweden
[6] Department of Biomedical Engineering, Rowan University, Glassboro, NJ, USA
[7] Department of Orthopaedic Surgery, Cooper Medical School of Rowan University, Camden, NJ, USA
[8] BioFrontiers Institute and Department of Chemical and Biological Engineering, College of Engineering and Applied Science, University of Colorado, Boulder, USA
[9] Senior authors
[‡] Authors contributed equally
[*] Correspondence: john-robert.davis@manchester.ac.uk (JRD), c.dunlop@surrey.ac.uk (CD), and nic-tapon@crick.ac.uk (NT)

Abstract

For tissues to develop and maintain their function, cells must orchestrate their behaviour by generating and transmitting contractile forces. These forces are transmitted to their surrounding matrix or neighbouring cells via adhesion complexes. How tissues reach a force-balance is often assumed to involve intercellular stresses counterbalancing those in the substrate. However, experimental findings indicate that dampening focal adhesions can increase intercellular stresses. As the ECM is rarely uniform in composition or mechanical properties, it is important to understand how focal adhesions alter stress transmission and the force-balance of a tissue. To address this, we confined monolayers on disk or ring adhesive patterns to alter how they were bound to the substrate. Traction force microscopy and laser ablations of cell-cell junctions were used to examine stresses across epithelial monolayers whilst modulating substrate stiffness. We show that monolayers reach different force-balance states depending on focal adhesion distribution, with intercellular stresses not correlated with overall traction stresses on rings. Using an active matter model to examine the force-balance dynamics, we reveal that tissues reach a force-balance by generating non-uniform patterns of contractility linked to adhesion patterning. This work highlights the importance of considering the position and mechanical properties of cell-ECM and cell-cell attachments to capture the mechanical landscape of living tissues.

49 **Main**

50 A key aspect of many developmental, physiological, and pathological processes is the
51 ability of cells to generate and transmit forces across a tissue. Cells mainly generate
52 contractile forces through their actomyosin cytoskeleton, which are then transmitted to the
53 environment through adhesion complexes[1]. Stress transmission is essential for orchestrating
54 cooperative cell processes such as morphogenesis[2], collective migration[3] and wound
55 healing[4]. Stresses are transmitted across adhesion complexes to either the substrate or
56 neighbouring cells[2]. As epithelial cells have both cell-substrate and cell-cell adhesions, they
57 must balance these different modes of stress transmission to drive the appropriate
58 behaviours. However, at present we do not have a clear understanding of the relationship
59 between stresses transmitted across cell-substrate or cell-cell adhesions in epithelia.

60 Various methodologies are available to interrogate cell-derived forces within
61 tissues[5]. Traction force microscopy, where the movement of microbeads embedded within a
62 substrate is tracked, is a proven method for examining cell-generated forces transmitted to
63 the substrate[6]. Examining traction forces of cell doublets[7–9], small cell clusters[10] and
64 epithelial sheets[11,12] revealed local stress imbalances, suggesting an internal force balance
65 must be reached within the cell assemblies. Following intuition based on mechanical
66 arguments, unbalanced cell-substrate traction forces are proposed to be transmitted across
67 cell-cell junctions[7,10,11,13]. Assuming even contractility across cell doublets or small cell
68 clusters, intercellular stresses were inferred with force balance equations based on traction
69 data. This yielded a positive correlation between traction forces and intercellular stress,
70 with increased tractions leading to greater intercellular stresses[7,10]. There is some
71 experimental data supporting this model, tension sensors for different cell-cell adhesion
72 molecules based on Förster resonance energy transfer (FRET), have shown increased
73 molecular tension in monolayers cultured on stiffer substrates[14,15]. However, it has also
74 been reported in cell doublets, that cell-cell forces inferred from traction force data do not
75 correlate with the FRET-efficiency of an E-Cadherin tension sensor, with the authors
76 suggesting a molecular tension homeostasis[9]. Furthermore, laser ablation experiments in
77 various biological systems are inconsistent with a simple proportional relationship between
78 traction and intercellular forces.

79 Laser ablation is a widely employed technique to quantify junctional tensions within
80 tissues and through rheological models infer tissue mechanical properties. This is achieved

81 by examining the relaxation of cells after individual or groups of junctions have been cut[16,17].
82 By disrupting entire cell-cell junctions, this method provides a holistic overview of cell
83 mechanics incorporating both cortical cytoskeleton and all cell-cell adhesion dynamics. It is
84 the gold-standard approach in developmental systems that are not amenable to other types
85 of biomechanical techniques to measure or infer tissue mechanics. Laser ablation of
86 amnioserosa cells during *Drosophila* embryonic dorsal closure revealed that focal adhesions
87 act as tethers that limit intercellular stress transmission[18]. Furthermore, work in the
88 *Drosophila* abdominal epidermis showed that degradation of the basal ECM occurring at the
89 pupal stage dramatically reduced cell-substrate friction without eliciting a commensurate
90 drop in intercellular tension[19]. These observations are not limited to developing tissues:
91 Madin-Darby canine kidney (MDCK) cells cultured on large micropatterned disks show
92 higher tension on softer hydrogels where cell-ECM attachments are weaker compared with
93 stiffer hydrogels[20]. However, the role of focal adhesions in this example was thought to
94 impact cell spreading after cell divisions[20]. Taken together, these studies suggest that cell-
95 substrate adhesions can limit rather than promote stress transmission across cell-cell
96 adhesions. It is therefore important to understand what role focal adhesion arrangement
97 plays in tissues acquiring a force-balance. This is especially true when considering that ECM
98 composition, architecture and mechanical properties are heterogeneous[21]. Furthermore,
99 the ECM is dynamic *in vivo*, especially during development[22] and wound healing[23], and local
100 remodelling can elicit changes in cell behaviour leading to diseases such as cancer[24].
101 Here, we combine traction force microscopy and laser ablation to examine the
102 generation and transmission of stresses across both the substrate and cell-cell adhesions. As
103 traction forces are known to be dependent on the size and geometry[25,26] of cells and tissues,
104 we employed micropatterning of hydrogels to standardise these factors. To examine the
105 role of focal adhesions in determining a tissues mechanical equilibrium we cultured
106 monolayers on disks or rings limiting the adhesive surface area. To alter stresses generated
107 by the monolayers, we modulated substrate stiffness which is known to regulate traction
108 forces[25]. When focal adhesions are distributed throughout the monolayer, traction force
109 generation and stress transmission are dependent on the substrate stiffness within our
110 experimentally tested range. However, when focal adhesions are restricted to the
111 monolayer periphery, traction forces become independent of substrate stiffness and stress
112 transmission occurs mainly through the monolayer. Furthermore, we observe that

intercellular stress is inversely proportional to substrate stiffness, so that intercellular stress reduces as stiffness increases. Through theoretical modelling and experimental observations, we show that this relationship between substrate stiffness and intercellular stress is elicited by the emergence of non-uniform contractility across the monolayer, with greater contractility present at regions with greater adhesions.

119 **Results**

120

121 Adhesive surface area dictates focal adhesion patterns across a monolayer

122 To examine the effect of the environment on stress transmission across a
123 monolayer, we cultured non-tumorigenic mouse mammary epithelial cells (EpH4)[27] on
124 methacrylated hyaluronic acid (MeHA) hydrogels[28]. 3% w/v MeHA solutions were
125 crosslinked with a range of dithiothreitol (DTT) crosslinker concentrations to modulate the
126 rigidity of hydrogels from 10.8 $\pm$ 2.5 kPa to 31.4 $\pm$ 2.8 kPa at intervals of ~5kPa (Extended
127 data Fig. 1a-c). These values are higher than what has been reported for mouse mammary
128 tissue[29] but span the reported basement membrane range[21] and a range from physiological
129 to disease state in human breast tissue[30]. ECMs are heterogenous and dynamic[21,22], and it
130 can be absent from tissues altogether[19]. We therefore wanted to modulate the adhesive
131 surface area beneath monolayers to mimic states where the matrix is present or absent. For
132 this purpose, we micropatterned MeHA hydrogels with laminin, the EpH4's preferred ECM
133 component[31], either as a disk (Fig. 1a) or ring (Fig. 1b). The diameter of the micropatterns
134 was 200μm (approximately 10 – 20 cells wide) with the width of rings being 20μm
135 (approximately 1-2 cells wide). We conjugated Alexa633 fluorophore to laminin to assess if
136 increasing levels of MeHA crosslinking increased the concentration of laminin on the surface
137 of hydrogels for both disk (Fig. 1c) and ring (Fig. 1d) patterns. Whilst there were fluctuations
138 in laminin intensity on different hydrogel stiffnesses (Fig. 1c,d) and radially across the disk
139 pattern (Fig. 1c), this did not correlate with differences in focal adhesions (Fig. 1g,h).
140 Therefore, the concentration of laminin in patterned areas did not limit the adhesions that
141 cells can generate with the substrate.

142 To measure active focal adhesions on different patterns, we immunostained
143 monolayers for phosphorylated focal adhesion kinase (pFAK) (Fig. 1e,f). Altering the
144 adhesive surface did lead to changes in the distribution of pFAK across the monolayer. On
145 disks, pFAK was evenly distributed across the entire monolayer with a slight peak at the
146 periphery of the monolayer (Fig. 1g). On rings however, pFAK was mainly focused on the
147 perimeter of the adhesive area with peaks at the boundary, with a low-level present in the
148 non-patterned area (Fig. 1h). As no laminin is present in the middle of the ring
149 micropatterns (Fig. 1d), there are two possible explanations that could explain the presence
150 of adhesions in the non-patterned region. The first is that cells adhere to non-modified

151 hyaluronic acid present in the MeHA hydrogel[32], and the second, that EpH4 cells deposit
152 nascent proteins[33,34]. As our modification rate was between 76 – 79% (Extended Data Fig.
153 1a) far higher than the threshold for cells to bind to unmodified disaccharides, it is more
154 likely that cells are binding to nascent proteins. Whether these nascent peptides allow force
155 transmission into the substrate is not clear. On disks, most cells across the monolayer are
156 surrounded by pFAK (Fig. 1c), whilst on rings, cells in the centre tended to only have isolated
157 puncta of pFAK and at the patterned region pFAK was mainly localised at the laminin-
158 positive edges (Fig. 1d,h). Examining the total pFAK coverage beneath disks and rings
159 revealed that rings consistently had less total pFAK coverage than disks, and both patterns
160 showed a slight reduction as substrate stiffness increased (Extended Data Fig. 1d,e). The
161 regulation of focal adhesion dynamics is dependent on many factors[35], and there are
162 contradictory reports on how substrate rigidity alters focal adhesion coverage[36,37]. Most of
163 these studies examine single cells rather than monolayers, therefore it is not clear why total
164 pFAK coverage reduces on stiffer hydrogels. However, cells have been reported to sense
165 and respond to strain energy and not substrate rigidity[38], and as we are examining active
166 focal adhesions it is possible that strain energy is reducing in our system. In summary, we
167 established experimental conditions that allow us to vary adhesive surface distribution and
168 substrate stiffness.
169 We next examined if altering the adhesive pattern or substrate rigidity altered cell-
170 cell adhesions or cell morphology across the monolayer. We observed no obvious
171 differences in the localisation of E-Cadherin for both patterns on all hydrogel stiffnesses,
172 with strong localisation along entire cell boundaries (Fig. 1e,f). Likewise, whilst there was a
173 distribution in the number of cells that composed each monolayer, the distribution was the
174 same for all patterns and substrate rigidities (Fig. 1i,j). Examining cell morphology, we
175 observed that cell height does not significantly change as substrate rigidity increases (Fig.
176 1k,l). However, we did observe that whilst on disks height is relatively constant (8.9 ±
177 1.3μm; Fig. 1k), on rings height increases from 8.9 ± 1.8μm in the centre to 10.4 ± 1.8μm on
178 the adhesive area (Fig. 1l). Cell area tended to be slightly higher in the centre of the
179 patterns, especially for disks (Extended data Fig. 1f,g) whilst there tended to be a slight
180 increase in elongation at the perimeter for both patterns (Extended data Fig. 1h,i). However,
181 there was no clear differences in cell morphology between the different patterns suggesting
182 that packing was not affected by limiting the adhesive surface.

Finally, we examined how stable cell-cell junctions were over our experimental timescales, or whether there was a high degree of junctional instability. For our movies, we imaged for one minute before performing laser ablations, so subtracted the frame prior to laser ablation from the initial frame and calculated the percentage pixel intensity that remained. This analysis revealed a value close to zero on both patterns and on all hydrogel stiffnesses (Extended Data Fig. 1j,k). Furthermore, overlayed images of cell membranes for the same duration as our ablation experiments (5 minutes apart), showed a high degree of overlap (Extended Data Fig. 1l). We therefore assume that junctional rearrangements is not a major contributing factor to the force balance dynamics of the monolayer.

Focal adhesion patterning alters dependence of traction forces on substrate stiffness

We next wanted to assess how altering the adhesive area affected traction forces. To measure traction forces, we embedded fluorescent microbeads within the MeHA hydrogels and measured their displacement[39]. Following recent reporting of extensile forces generated by MDCK cell layers[20], we first confirmed that all displacement vectors indicated contraction towards the centre of the cell layer across all substrates (Fig. 2a,b, Extended Data Fig. 2a-d). We also observed the greatest displacements at the periphery of the monolayer (Fig. 2a,b, Extended Data Fig. 2e,f). As expected from previous reports[20,25], we observed a reduction in displacement magnitude as substrate rigidity increased for both disks and rings (Fig. 2c,d, Extended Data Fig. 2g-h). We next examined the traction forces generated by the monolayers and noticed stark differences between disk and ring patterns (Fig. 2e-h). On disk patterns we observe a decrease in both total traction forces and the maximum traction force as substrate stiffness increased (Fig. 2e,g). On rings, total traction force remained almost constant (Fig. 2f), and maximum traction forces showed a weak reduction (Fig. 2h). It has been reported in micropatterned single MDCK cells that strain energy is not affected by substrate rigidity[25]. In the case of the monolayers considered here, as displacement decreased for both patterns, but traction forces only decreased for disk patterns, we were interested in examining if our adhesive patterns showed marked differences in strain energy. We observed that for both disks and rings there is a decrease in strain energy as substrate stiffness increases but that this difference is stronger for disks than it is for rings (Fig. 2i,j); with a mean strain energy reduction from 10kPa to 30kPa for disks (25,242pJ) being almost double that of rings (13,481pJ). As the traction forces

215 highlighted a clear difference in behaviour between disk and rings on different substrates,
216 we decided to examine whether this reflected a difference in the spatial distribution of
217 traction forces. Examining mean traction forces radially along the epithelial clusters showed
218 the highest traction forces at the periphery for both ring and disk patterns on all substrates
219 (Fig. 2k,l). Consistent to the changes in total and max traction forces, for disks we observe a
220 reduction in traction magnitude with increasing stiffness whilst on rings we observe virtually
221 no change in traction force magnitude (Fig. 2k,l). However, we noticed a slight change in the
222 distribution of traction forces radially between the patterns, with traction forces appearing
223 to be more localised at the periphery on rings than in disks especially on soft substrates (Fig.
224 2k,l). As our pFAK data shows on disks all cells our surrounded by focal adhesions, this
225 suggests that cells within the monolayer locally contribute towards deforming the substrate,
226 leading to a gradual radial accumulation in traction forces. However, as the hydrogel
227 becomes more rigid and cells are less able to deform the substrate, traction forces become
228 more localised to the edge, as previously theoretically predicted[40]. This is altered on ring
229 patterns where the cells in the central non-adhesive region do not deform the substrate
230 locally, so that the applied traction forces are always localised to the periphery. Taken
231 together our results suggest that altering the adhesive surface leads to changes in the
232 generation and distribution of traction forces across the epithelium.
233
234 Internal stresses decrease with increasing substrate stiffness
235 To interrogate stress transmission within the monolayer, we combined theoretical
236 and experimental approaches. The theoretical model developed describes the monolayer as
237 an active soft material in which the monolayer stresses and displacements are determined
238 from continuum elasticity theory, with the inclusion of an isotropic active stress in the
239 relationship between stress and strain that accounts for the cell-derived contractility (Fig.
240 3a, see Supplemental Information Table 1 for model parameters). Such active matter
241 models are widely adopted to describe active, contractile cells and tissues[25,40–42]. The
242 substrate is coupled into the model through force balance equations where an additional
243 resistance to contraction proportional to the displacement is included acting only where the
244 layer is adhered[40]. Based on our experimental observations with pFAK staining (Fig. 1i,j),
245 layers were either adhered uniformly to recapitulate the disk, or for the ring pattern, with
246 adhesions concentrated at the ring with an underlying distribution of small adhesions sites

247 everywhere else (Fig. 3a). A more detailed description of the model and the sensitivity
248 analysis can be found in supplemental information and methods section. As we observe a
249 reduction in total adhesion coverage as substrate stiffness increases (Extended data Fig.
250 1d,e), we examined with our model the sensitivity of total traction forces to different levels
251 of adhesion coverage (Supplemental Information). This revealed that traction forces
252 remained relatively constant with different levels of adhesion coverage above a 10%
253 coverage threshold (Supplemental Information Table 2). As the coverage of adhesions is
254 greater than 10% for all our conditions, we conclude that the reduction in adhesion
255 coverage we observe does not drastically limit the traction stresses generated by the
256 monolayer. As the monolayer was stable at the timescales measured (Extended Data Fig. 1k-
257 m), we considered the system to be in a stationary steady state and the forces balanced.
258 The model can be used to fit both the displacement data (Fig. 3b,c) and total traction
259 (Fig. 3d,e) for each substrate stiffness, with the cell-generated contractile stress as the fit
260 parameter. It was sufficient to assume the same uniform contractility for each cell across
261 the layer to reproduce the observed data, with small variations in overall contractile activity
262 on each stiffness. Extending this analysis, the internal stress within the layer, akin to
263 intercellular stress, can be determined from the force balance equations and as a reference
264 point, we plot the internal radial stress halfway across the radius (r=50μm; Fig. 3f,g). As
265 might be intuitively expected, the model predicts internal stresses that broadly follow the
266 same qualitative trends observed for total traction across both disks and rings. For the disks,
267 we predict a significant monotonic decrease as substrate stiffness increases, with the
268 greatest stresses being on the softer substrates (Fig. 3f). Whilst for the ring patterns, we see
269 that the stress remains broadly constant across the stiffnesses (Fig. 3g). We next sought to
270 examine experimentally whether the model's internal stress predictions were accurate by
271 considering both traction stresses using traction force microscopy and intercellular stresses
272 inferred from laser ablation.
273 We bisected the epithelial monolayers with an annular region of interest (ROI) (Fig.
274 3h)[16], and inferred bulk intercellular stresses by analysing the recoil velocity (Extended data
275 Fig. 3a,b). We observed that the greatest recoil was near the ablation site, and that vectors
276 were orientated away from the cut highlighting that the monolayers were always under
277 tension (Fig. 3i,j, Extended data Fig. 3c-f). Measuring the maximum recoil velocity half-life
278 revealed a similar relaxation time of ~20 ± 10s for both patterns and all stiffnesses. This

279 suggests that the viscoelastic properties of the monolayer weren't altered by focal adhesion
280 patterning or substrate stiffness (Extended data Fig. 3g-j), assuming that the Young's
281 modulus of cells is constant which has been shown to be independent of substrate
282 stiffness[44]. We then examined the maximum recoil velocity with respect to substrate
283 stiffness for both patterns. For the disk pattern, the recoil velocity showed a weak decrease
284 (Fig. 3k), qualitatively similar to the model predictions, but with the reduction in internal
285 stress being more subtle than that predicted (Fig. 3m). On ring patterns, while the model
286 predicts a constant recoil velocity, we observed a consistent decrease with increasing
287 stiffness (Fig. 3l). This reduction, which is not intuitively expected or predicted by the model,
288 suggests that a simple force balance with uniform mechanical activity does not describe the
289 system fully and that additional factors must be at play.
290 Comparing traction forces before and after ablation also revealed a reduction,
291 highlighting mechanical coupling of stresses within the monolayer to the tractions applied
292 to the substrate (Fig3o,p). Extending this analysis to the strain energy, we also observed a
293 reduction in strain energy after ablation on both patterns (Fig. 3q,r), with the exception
294 being for disks on the stiffest hydrogel where the was a negligible reduction (Fig. 3q). This
295 could be due to our imaging resolution as displacements measured for disks on 30kPa are
296 close to this range, and any small differences could be undetectable. As total traction and
297 strain energy vary for the different patterns and substrate stiffnesses, we examined the
298 percentage change to assess whether this reduction merely reflected the loss of cells in the
299 ablation region (Fig. 3o'-r'). This revealed there were differences in the percentage loss of
300 traction forces and strain energy (Fig. 3'-r'), which tended to be higher for rings than for
301 disks. Taken together, this supports the assumption that there is stress transmission from
302 cell-cell interactions which distributes forces into the substrate, and releasing intercellular
303 stress through ablation leads to a reduction in traction stresses generated by the
304 monolayer.
305
306 <u>Theoretical modelling suggests non-uniformity of contractility</u>
307 To illustrate the incompatibility of a model with uniform contractility , where all cells
308 generate equal forces across the monolayer, with the observed recoil velocities we focused
309 on the ring pattern which experimentally shows a constant total traction of ~53.7MPa (Fig.
310 2f) but a reduction in recoil velocity as substrate stiffness increased (Fig. 3l). For uniform

contractility (Fig. 4a) we examined how contractility (a) would have to be altered to maintain a constant internal stress (represented in blue) or total traction force (represented in red) as substrate stiffness increased. To orientate, we plotted an illustrative contour of constant internal stress at r=0.5 (which corresponds to the ablation region, blue line) and shaded the region below the contour which has a lower internal stress at r=0.5 (blue shaded region, Fig. 4a). Likewise, we also plotted an illustrative contour of constant total traction (red line) and shaded the region above the contour which has greater traction forces (red shaded region, Fig. 4a). Note that the shaded regions do not generate a practically relevant overlap, with uniform contractility (Fig. 4a), and a parameter sweep altering the contractility of the layer demonstrates that this is true for all physically relevant regimes (Supplemental information). This highlights that, as the system maintains a constant traction force (red contour) it does not encroach into the lower internal stress regime (blue shaded region). Likewise, to maintain a constant internal stress (blue contour) the system does not increase traction forces (red shaded region). This would inevitably lead to a system whereby changes in traction forces would lead to similar changes in internal stress as previously predicted (Fig. 3g,[7,10–12]).

These phase plane plots do suggest a potential resolution by considering a non-uniform distribution of mechanical contractility within the layer. By increasing contractility at the edges, the system generates an overlap region where it is possible to maintain total tractions but reduce internal stress (Fig. 4b). In the examples given, to maintain a constant internal stress within the layer (blue line) traction forces must increase as the blue contour now encroaches the shaded orange region, and similarly to maintain constant total traction forces (red line) the internal stress must decrease as it now encroaches the blue shaded region (Fig. 4b). As the latter example is similar to our experimental observations, we explored whether parameterising the mechanical gradient could reconcile theoretical predictions with experimental observations.

Introducing a new contractility function that generates monotonic increasing contractility. Specifically, we take P=$a(1 + br^n)$, as this enables analytical solution in restricted cases and simplifies the numerical solution, (see Supplemental Information). Here increasing b indicates more concentrated contractile activity at the edge (b=0 returns the model to uniform cell contraction). By parameterising the total contractility (P_{Total}) of the monolayer and distribution of contractility (b), we able to fit both tractions and internal

343 stress across the range of stiffnesses for both disk (Fig. 4c) and ring patterns (Fig. 4h).
344 Namely we find that the model can reproduce a large decrease in traction and slight
345 decrease in internal layer stress on disk patterns with increasing stiffness (Fig. 4d-f), while
346 also reproducing nearly constant total tractions and large decrease in internal layer stress
347 on the ring pattern as stiffness increases (Fig. 4i-k). Looking beyond the cell traction and
348 recoil data we considered the strain energy of the system. Non uniform contractility within
349 the model also reproduces the trends observed in the strain energy of both adhesive
350 patterns (Fig. 4g,l). With the disks where adhesion is uniformly distributed, the model
351 successfully captures the observed reduction in strain energy with increasing stiffness (Fig.
352 4g). For the ring pattern the model predicts a reduction in strain energy that qualitatively
353 fits the trend, however, with a more subtle level of reduction (Fig. 4l). This deviation in
354 strain energy at lower adhesion percentages is expected given the linear model of substrate
355 resistance to deformation (see Supplementary Information).
356 Significantly, we find a qualitative difference in behaviour between disk and ring
357 patterns for resolving experimental observations. For disk patterns the contractility must
358 become more uniformly distributed, with more cells sharing the work as stiffness increases
359 (Fig. 5a). However, on the ring pattern the opposite trend is required with the cells at the
360 edge of the layer being required to be more contractile compared with the rest of the layer
361 as stiffness increases, so that these edge cells then do the majority of the work (Fig. 5a).
362
363 Active myosin and F-actin are not uniformly distributed across monolayers
364 As our model suggested that non-uniformity of contractility could reconcile our
365 experimental observations, we decided to examine contractility within the monolayers. We
366 measured phosphorylated myosin light chain II (pMyoII) intensity across the monolayers as
367 a proxy for contractility, but also examined actin architecture which plays an essential role
368 in generating stresses[45]. As traction and intercellular stresses are dependent on myosin
369 activity[42,46], we initially wanted to examine if the total intensity of pMyoII altered depending
370 on the pattern and substrate stiffness. To minimise experimental variation, we processed all
371 independent samples in parallel to allow direct comparison in intensity using widefield
372 imaging for speed (Extended data Fig. 4a.b). Measuring the intensity of DAPI (Fig. 5b,c), we
373 observed consistent results with our cell count data (Fig. 1i,j). Examining F-actin revealed
374 that on disks there is a consistent level of F-actin, that appears to be linked to cell number

375 (Fig. 5d). However, on rings we observe a slight decrease in total F-actin intensity as
376 substrate stiffness increases (Fig. 5e). Next, we examined total intensity of pMyoII which
377 revealed a decrease as substrate stiffness increases, for both patterns but more pronounced
378 for rings (Fig. 3f,g). This is in agreement with our fitted model parameters which predicted
379 that there needed to be a reduction in contractility as substrate stiffness increased (Fig.
380 4c,h).

381 We did observe spatial variation in pMyoII to varying degrees on our monolayers
382 (Fig. 5h,i, Extended data Fig. 4a,b). As we observed minor radial differences in height on
383 rings (Fig. 1l) we wanted to examine pMyoII localisation within the monolayers for our
384 various conditions with optical sectioning, so employed confocal microscopy. pMyoII was
385 predominantly localised basally for both disks and rings (Extended data Fig. 4c-e), so we
386 focused our further analysis to this region (Fig. 5h-s). However, examining the whole
387 monolayer thickness shows similar but weaker trends (Extended data Fig. 4f,g).
388 Quantification of pMyoII intensity, normalised to the mean intensity in our ablation ROI (40-
389 50μm), revealed that no condition had a uniform localisation, with radial variation always
390 present (Fig. 5j,k). However, depending on the pattern and substrate stiffness there were
391 differences in the extent of non-uniformity across the monolayers. On disks, pMyoII
392 intensity was up to 10% greater at the periphery of the monolayers compared to the ROI on
393 the softest hydrogels but became more uniform as substrate stiffness increased (Fig. 5j). On
394 rings, there was a greater accumulation of pMyoII at the inner boundary of the adhesive
395 area in all conditions which became more pronounced as substrate stiffness increased (Fig.
396 5k). We next quantified the ratio in pMyoII radial intensity between the centre (<40μm) and
397 edge (>50μm) of the monolayer (Fig. 5l). For pMyoII, on disks the softest substrate showed
398 the greatest ratio (more concentrated to the edge) which plateaus to a more uniform
399 distribution on stiffer substrates (Fig. 5l). However, on rings, we see a reversal of this trend
400 with the stiffer substrates showing the greatest radial distribution (Fig. 5l). Taken together,
401 we observe radial variation in pMyoII localisation and actin architecture, in accordance with
402 our conclusions from the model that contractility must have a radial distribution to
403 reconcile our experimentally observed traction and intercellular stresses. Furthermore, the
404 parameterisation predictions that on disks radial contractility must become more uniform
405 on stiffer substrates whilst on rings the opposite must occur also holds true in experimental
406 observations (Fig. 4c-h and 5l).

Overall, reconciling the model and experimental observations suggests that across the monolayer, the transmission of forces between cells generates internal stress such that the cell-substrate adhesion and traction forces do not follow simple counterbalancing relationships. Instead, the distribution of contractility adapts to generate a whole tissue mechanical force balance, which is dependent on the distribution of focal adhesions across the tissue.

413 **Discussion**

414 The control of a tissue's mechanical equilibrium is essential for the regulation of a
415 wide array of physiological processes such as morphogenesis[2], wound healing[4], and when
416 disturbed can lead to disease progression[47]. Here we describe for epithelial monolayers, the
417 role of focal adhesion distribution in reaching a mechanical equilibrium. Through
418 experimental observations, we found on ring patterns where focal adhesion distribution is
419 non-uniform, that epithelial monolayer stresses do not conform to intuitions on force-
420 balance, namely that traction and intercellular stresses are proportionally counterbalanced
421 (Fig. 3m,n). To reconcile experimental observations with monolayers being at force-balance,
422 we proposed and confirmed that spatial patterns in contractility emerge. Whilst spatial
423 distribution of contractility has been observed in single cells[48,49] linked to focal adhesion
424 signalling[48], to our knowledge this has not been reported for monolayers. Furthermore,
425 often active matter models assume that contractility is uniform across a tissue. Whilst
426 spatial variation in myosin have been observed in tissues, these are generally localised to
427 cell-population boundaries[50] or in specific populations for morphogenesis[51,52]. However, we
428 recently observed in *Drosophila* histoblasts that a tissue-wide spatial pattern of myosin
429 develops during the pupal stages[19] but whether this is important for the tissue's mechanical
430 equilibrium is not known.

431 What mechanisms lead to these spatial patterns of contractility? Whilst not directly
432 examined here, we can speculate based on mechanobiology arguments. Cells sense their
433 environment and tissue stresses through mechanotransduction mechanisms and modulate
434 their contractility to achieve a mechanical equilibrium[47]. Each cell generates contractile
435 forces through the actomyosin cytoskeleton, which when linked to adhesions transfers this
436 force to the local environment[2]. Forces can be transferred through cell-cell or cell-ECM
437 junctions but whether they are transmitted across a tissue is dependent on the mechanical
438 properties of neighbouring cells and the ECM. For example, blocking stress transmission
439 through cells by disrupting cell-cell junctions leads to a redistribution of traction stresses,
440 from localised at the periphery of cell clusters to locally around each cell[53,54]. Likewise,
441 induction of E-Cadherin expression leads to traction forces becoming radially organised and
442 larger, as cells globally increase pMyoII[55]. Therefore, cell-cell junctions enable long-range
443 stress transmission through a tissue. Likewise, the physical properties of the ECM can alter
444 stress transmission through a tissue. Avian fibroblasts remodel the ECM through

445 contractility, and diminishing tissue-scale stress transmission by cross-linking the ECM
446 blocks the emergence of supracellular ordered behaviours[56]. Therefore, when considering
447 how mechanotransduction might affect cellular processes across a tissue, it is important to
448 understand how forces are both locally transferred to the surroundings and transmitted
449 across a tissue.

450 In comparison with single cell studies, in large clusters of cells a range of possibilities
451 for how stress can be transmitted within the tissue and to the substrate open-up. Here, we
452 observe that monolayers alter their contractility spatially as cells respond to their
453 mechanical environment, and this deviates between ring and disk patterns as substrate
454 stiffness increases. We can reason why this is the case, assuming that on our disk patterns
455 cell-generated forces are dominated by focal adhesions and not cell-cell junctions. This
456 seems a reasonable assumption given the flat morphology of our cells (Fig. 5c),
457 accumulation of pFAK near cell-cell junctions (Fig. 1e), and that actin architecture appears
458 connected to focal adhesions (Extended data Fig. 4h) which has been reported to determine
459 stress transmission[42,5718–20]. On soft hydrogels, where we observe the greatest radial
460 distribution in pMyoII on disks, cells can locally deform the substrate (Extended data Fig. 2),
461 allowing forces to be transmitted across the monolayer through both the hydrogel substrate
462 and cell-cell adhesions (Fig 3). We speculate that in soft conditions, a high proportion of cell-
463 generated forces are transmitted across the monolayer, leading to higher contractility (Fig.
464 5f) and the radial increase in contractility towards the periphery as cells sense the
465 accumulation of stresses transmitted. However, on stiff substrates cells are no longer able
466 to locally deform the substrate (Extended data Fig. 2), limiting stress transmission through
467 the substrate. We speculate that in this situation, cells locally transfer forces to both the
468 substrate and neighbouring cells. However, this can only be transmitted across the
469 monolayer through cells, with this transmission dampened by restrictions of local ECM
470 attachment, leading to a more uniform contractility. For our ring micropatterns, only the
471 most peripheral substrate adhered cells can transfer forces to the substrate as well as cell-
472 cell junctions, with the bulk of the monolayer transferring solely through cell-cell adhesions.
473 This is emphasised by the fact the loss in traction forces and strain energy tends to be higher
474 on rings than disks (Fig. 3o-r) highlighting that the central cells are contributing more to
475 these variables. This leads to a scenario where focal adhesions do not dominate the transfer
476 of forces to the local surroundings, and non-local effects emerge through long-range stress

477 transmission leading to an integrated tissue. On soft hydrogels, we speculate that peripheral
478 cells transmit forces transferred to the substrate to neighbouring cell-cell junctions due to
479 its compliance. This then leads to global substrate sensing and an increase in contractility
480 globally (Fig. 5l). However, on stiffer substrates this global substrate sensing is lost, as the
481 rigidity of the substrate limits peripheral cells transmitting their generated forces to their
482 neighbours, and cells reduce their contractility. However, the peripheral cells are still
483 sensing the forces transmitted by the central cells across cell-cell junctions, as well as the
484 substrate, and therefore increase their contractility.

485 The emergence of spatial patterns of contractility in our monolayers has important
486 implications on the application of force inference techniques. To examine intercellular
487 stresses of a monolayer, inference methods such as monolayer force microscopy (MSM)[11–13]
488 or Bayesian inversion stress microscopy (BISM)[58] have been developed. These techniques
489 infer intercellular stresses based on traction forces measured and can estimate spatial
490 variation in intercellular stresses in a non-destructive manner, unlike laser ablation, allowing
491 long-term analysis to be made. Often the implementation of these techniques assumes a
492 counterbalance between traction and intercellular stresses[10,12,13,42,59]. For MDCK cell-
493 doublets, where focal adhesions have been shown to disassemble along cell-cell contacts[60],
494 the direct balance of traction forces with cell-cell adhesions potentially holds[7]. However,
495 even in these simple cell-doublet systems the distribution of focal adhesions can drastically
496 alter the propagation of forces. For instance, cardiomyocyte doublets seeded or cultured on
497 90kPa substrates generated focal adhesions at the site of cell-cell junctions, impairing
498 mechanical coupling and force propagation[8]. This highlights the importance of examining
499 the distribution of focal adhesions when inferring stress transmission. Moreover, on our
500 200μm diameter disk micropatterns, we observed spatial variation in pFAK with some
501 regions having higher intensity than others (see Fig 1c). Considering a larger tissue, the
502 distribution of focal adhesions could vary drastically even on a uniform substrate, altering
503 the local mechanical equilibrium in that region of a tissue. This would impact on whether
504 local intercellular stresses were positively correlated with traction stress or not. Indeed,
505 analysis of epithelial monolayers showed a “rugged landscape” of traction forces[12], and
506 spatial patterns of ECM composition and properties have been observed in developmental
507 and pathological situations[21]. Therefore, when employing techniques such as MSM and

BISM it is important to examine the variation in local distribution of focal adhesions to confidently infer intercellular stresses.

513 **Methods**
514
515 **Cell culture**
516 EpH4 cells with Cas9 inserted into the Rosa26 locus (kind gift from high throughput
517 screening STP, Francis Crick Institute) were cultured in 4.5g l^{-1} Dulbecco's modified Eagle
518 medium (Gibco, Thermo Fisher Scientific) containing 10% foetal bovine serum (Sigma-
519 Aldrich, Merck) and 1% penicillin-streptavidin (Gibco, Thermo Fisher Scientific). For seeding
520 on hydrogels, 180,000 cells in 2ml of culture medium were centrifuged at 80 r.c.f for 5
521 minutes. Cells were cultured for 2 hours and then extensively washed in PBS to remove non-
522 adherent cells and 2ml of fresh media was added. Cells were incubated for 48 hours, to
523 proliferate and cover the micropatterns. For live-imaging experiments, cells were washed in
524 PBS and then labelled for 15 minutes with 1.5μl CellMask Green (Thermo Fisher Scientific),
525 diluted and vortexed in 1.5ml FluoroBrite DMEM (Gibco, Thermo Fisher Scientific)
526 containing 1% penicillin-streptavidin but no FBS. Media was then replaced with 1.5ml
527 FluoroBrite DMEM media as described, ready for imaging.
528
529 **Micropatterning of methacrylated hyaluronic acid hydrogels**
530 3g of methacrylated hyaluronic acid (MeHA) was synthesised as previously described[28], with
531 a methacrylate modification of hyaluronic acid monomer between 76 – 79% as
532 characterised through ^{1}H NMR (Extended Data Fig. 1a). MeHA hydrogels were formed at a
533 concentration of 3 wt% and crosslinked with increasing amounts of dithiothreitol (DTT) to
534 modulate substrate rigidity. Specifically, hydrogels were formed within a 250μm high silicon
535 gasket with a 16mm inner diameter and outer diameter of 18mm, sandwiched between a
536 19mm micropatterned coverslip and a silanized glass surface. Hydrogels were incubated
537 with 5% BSA (Tocris Bioscience) in PBS for 2 hours before seeding cells.
538
539 Micropatterned coverslips were generated by plasma-activating 18mm coverslips and
540 coating in 0.1mg ml^{-1} poly-L-lysine poly(ethylene glycol) (PLL(20) – g[3.5]-PEG(2), SuSoS)
541 suspended in 10mM HEPES buffer at pH7.4. To pattern the coverslips, a quartz photomask
542 (Compugraphics) and UVO-cleaner (Jelight) were used to remove PLL-g-PEG from the
543 surface of the coverslip. Patterned coverslips were then incubated for 30 minutes with
544 laminin diluted in 100mM sodium bicarbonate buffer at pH7.4. Laminin consisted of either

545 20μg ml^{-1} laminin (Sigma-Aldrich, Merck) solution or 20μg ml^{-1} 2:1 mix of laminin and
546 laminin-labelled with alexa633 for live-imaging and immunostaining, respectively. To label
547 laminin, 500μl of 1mg ml^{-1} laminin solution was injected into a Slide-A-Lyzer (Thermo Fisher
548 Scientific) and dialysed two times in 1L of PBS at 4°C and stirred at a low shear rate for 24
549 hours. The dialysed laminin was then labelled with Alexa633 following the manufacturers
550 protocol (Thermo Fisher Scientific). Micropatterns were either repeating patterns of disks
551 with a diameter of 200μm, or rings with an outer diameter of 200μm and inner diameter of
552 160μm.
553
554 For silanized glass surfaces, either No. 1.5 glass bottom 35mm μ-dishes high (Ibidi) or 20mm
555 diameter uncoated 6-well plates (Mattek) were employed for live-imaging or
556 immunostainings, respectively. Glass surfaces were plasma-activated and silanized with (3-
557 aminopropyl) trimethoxysilane (VWR) and 5% glutaraldehyde (VWR).
558
559 **Atomic force microscopy**
560 Gels were generated as described but using non-patterned, passivated coverslips and No.
561 1.5 50mm dish with 30mm uncoated glass diameter (Mattek). Force curves were measured
562 on a JPK Nanowizard 4 using a CP-qp-CONT-Au-B-5 cantilever probe (sQube, NanoAndMore
563 GMBH). Measurements were taken in four regions per hydrogel (two at the periphery and
564 two central) with 50 indentations over a 100μm x 100μm grid. The number of hydrogels
565 quantified for each DTT concentration was 7 for 6.30 to 15.75mM and 6 for 18.9mM. Force
566 curves were made with an extend speed of 2μm s^{-1} and a setpoint (8 – 25nN, depending on
567 substrate stiffness) set to achieve a maximum indentation depth of ~500nm. The young's
568 modulus was calculated by fitting a Hertz model using the AFM_Youngs_modulus_fit
569 programme developed by Dr Stefania Marcotti (available on GitHub), at different
570 indentation depths (Extended data Fig. 1b). A standard indentation depth of 250nm across
571 all hydrogel conditions was used to calculate the Young's modulus, as it is within the linear
572 phase of the modulus versus indentation depth for all hydrogel conditions and is 1/1000 of
573 the hydrogel thickness (Extended data Fig. 1c).
574
575 **Traction force microscopy**

576 Crimson labelled 0.2μm carboxylate modified FluoSpheres (Thermo Fisher Scientific) were
577 mixed with MeHA hydrogel precursor solution with a 1:40 ratio prior to crosslinking with
578 DTT. Images were acquired as detailed below. After live-imaging, cells were treated with 10x
579 trypsin-EDTA, no-phenol red (Gibco) until cells detach from the hydrogels and a final
580 reference frame acquired.
581
582 **Laser ablation**
583 Images were acquired on a Zeiss LSM 780 system with an LD C-Apochromat 40x NA 1.1
584 water objective and 0.8 zoom, so that micropatterns could be acquired in a single 512 x 512
585 pixel tile. Z-stacks were acquired by measuring excitation by 480nm and 633nm lasers
586 simultaneously for z-slices every 1μm, spaced between 5 - 6μm below the hydrogel surface
587 and 10 - 12μm above. Z-stacks were acquired every 10 seconds for one minute before a
588 laser ablation and five minutes afterwards. An annulus ROI was generated using the
589 freehand tool and had an internal diameter of 80μm (154 pixels) – approximately 4 – 6 cells
590 in diameter – and external diameter of 100μm (193 pixels) – leaving 3 – 4 cells at the
591 periphery. Ablations were made in a z-plane positioned in the middle of the epithelial layer
592 (3 - 6μm from the hydrogel surface) with a Coherent Chameleon NIR tuneable laser set at
593 780nm and 40% - 60% power output and lasted ~6.7ms.
594
595 **Immunostaining**
596 Samples were fixed in 4%-paraformaldehyde (TAAB) for 15 minutes and permeabilised with
597 0.3% Triton X-100 for 5 minutes, covered from light. Samples were then blocked with 10%
598 neonatal goat serum (Generon) for an hour at room temperature and incubated with
599 primary antibodies diluted in 10% neonatal goat serum at 4°C overnight. Samples were then
600 incubated in secondary antibodies, Phalloidin-Alexa568 (Thermo Fisher Scientific, #A12380:
601 dilution 1:400) and DAPI (1000x stock solution; Sigma) for 1 hour at room temperature.
602 Samples were washed and stored in 0.1% Triton X-100. For batch processing of all samples
603 to examine total pMyoII levels, images were acquired on a Zeiss Celldiscoverer 7 widefield
604 system with a Zeiss Plan-Apochromat 20x NA 0.7 Autocorr objective with 1x zoom and 2240
605 x 2254 pixels and a x-y resolution 0.1747602 for a single plane. To examine spatial
606 localisation of proteins of interest, samples were imaged on a Nikon CSU-W1 spinning disk

607 with an Apo LWD 40x WI λS DIC N2 NA 1.15 objective with 1200 x 1200 pixels and a x-y
608 resolution of 0.2731993μm. Z-slices were acquired 0.4μm apart for each channel
609 sequentially. The following antibodies were used, mouse anti-phospho-Myosin Light Chain 2
610 (Ser19) (Cell Signalling Technology, #3675: dilution 1:200), rabbit anti-phospho-FAK (Tyr397)
611 (Thermo Fisher Scientific, 44-624G: dilution 1:400), mouse anti-E-Cadherin (BD Transduction
612 #610182: dilution 1:400), Goat anti-mouse IgG H&L Alexa 405 (Abcam, #175660: dilution
613 1:400), and Goat anti-rabbit IgG H&L Alexa 488 (Thermo Fisher Scientific, #A-11008: dilution
614 1:400). F-actin was stained with Alexa Fluor 568 Phalloidin (Thermo Fisher Scientific, #A-
615 12380) along with the secondary antibodies.
616
617 **Data analysis**
618 All images were processed and analysed in Fiji, Matlab and Wolfram Mathematica.
619
620 Traction force microscopy pipeline
621 Images were acquired as detailed above. After adding trypsin to detach cells, there is slight
622 stage movement in the in x, y and z directions. Therefore, all movies were registered with
623 the trypsin frame as a reference. For z registration, the surface of the hydrogel was
624 calculated by examining the total intensity across the image in 24x24 pixel blocks for each z-
625 slice, with the surface for each block set by the last frame with a signal. To project on a
626 pixel-by-pixel basis, a Gaussian Filter was employed across all blocks and then rounded, to
627 minimise any jumps in z-plane. A maximum projection of the beads was then calculated for
628 both the movie and trypsin reference frame from the surface to the same number of z-slices
629 below the surface set by the least number of frames available, normally 3 - 4 slices. Once z-
630 registration is complete the trypsin frame was added as the final frame of the movie and
631 registered in Fiji with the StackReg macro, using the last frame as the reference. Bead
632 displacement, traction forces and strain energy were calculated using the TFM package
633 developed by Gaudenz Danuser's group[39], using a 31x31 pixel template size and L-
634 parameterisation of 0.00000001.
635
636 Laser ablation analysis
637 Initially a projection of the cell mask was generated by identifying the ablation plane and
638 calculating a maximum projection between two slices above and below this frame. The

639 ablation plane was identified by measuring the loss of intensity within the ablation ROI for
640 each frame after the ablation and selecting the frame with the biggest loss. To measure the
641 recoil velocity, the Mathematica ImageFeatureTrack function was employed with specifying
642 features in every pixel and filtering pixels where no motion was detected. To measure
643 maximum recoil velocity for each movie, the recoil velocity value for the 95th percentile
644 across the entire field of view was taken (see Extended Data Fig. 3).
645
646 Cell morphology quantification
647 To measure cell elongation and area, projections generated for analysing the recoil velocity
648 were segmented through Skeletor[19] and manually corrected in Fiji. Using a watershed
649 algorithm in Mathematica, cell area and elongation (1-width/length) were measured. To
650 measure cell height, all immunostaining experiments were combined, and an orthogonal
651 projection made using the Fiji macro with a box ROI 20 x 850 pixels centred on the
652 monolayer centroid in both the x and y direction. In Mathematica, cell height was measured
653 by combining F-actin intensity with either pMyoII or E-Cad intensity for the orthogonal
654 projections, depending on the experiments, and binarizing based on pixels whose intensity
655 was greater than the mean plus four standard deviations of the entire projected image. A
656 FillingTransform and DeleteSmallComponents function were applied to clean up the
657 binarization so only the monolayer remained.
658
659 Membrane intensity changes
660 To measure the movement of the epithelium in our movies before the ablation to
661 determine their dynamics, the frame immediately before the ablation was subtracted from
662 the initial frame and the remaining pixel values summed and normalised to the original
663 summed pixel values. A value close to zero highlights very little movement within the
664 epithelium.
665
666 Basal projection algorithm
667 To quantify just the basal layer of the monolayers we used Laminin labelling to identify the
668 surface of the hydrogel. We selected a z-slice for each pixel that corresponded to the
669 highest laminin intensity, after noise-filtering the z-intensity profile with a LowpassFilter. We
670 then generated a contour map by smoothening the pixel values with a GaussianFilter,

before rounding to a whole number to correspond to a z-slice. Based on this contour map, we then did a maximum projection over three z-slices, one above and one below our contour map value.

pFAK segmentation

To quantify adhesion coverage and size, pFAK images were binarized based on pixel intensity value in Mathematica. Due to variable background intensity across the field of view, a MedianFilter was applied with a 61 pixel-by-pixel sliding window and subtracted from the original image. A background threshold value was then calculated by measuring the mean intensity plus two standard deviations of pixels outside the micropatterned region which was determined based on the laminin micropattern channel. Any pixel which had a higher intensity value than the background threshold was binarized. To de-noise the binary image, isolated binarized pixels were removed using the DeleteSmallComponents function with a value set to 1.

Statistical analysis

All statistics were performed in Mathematica using the LocationEquivalenceTest function which tests the null hypothesis that populations are equal choosing the most powerful test that applies to the data. The most common test applied was the Kruskal Wallis test as often one condition would fail normality tests. If the LocationEquivalenceTest was significant a post-test Mann-Whitney was performed comparing the value on the softest substrate to all other substrate stiffnesses. For trend fitting, the LinearModelFit function was used on the mean values for each population with a confidence interval of 95%. The model with the greatest R^2-value was selected.

For all statistical values used in the analysis, see Extended data tables.

Theoretical modelling

We describe the theoretical and computational modelling briefly here, for a more detailed description see the additional supplementary information.

Active matter model for the cell layer

An active matter model was used to predict the deformations and stresses in the cell layer. This widely adopted approach incorporates an active cell-generated stress additively into the constitutive relation of the cell material, see[40,61–63]. As such we assumed a constitutive relation such that the stress $\sigma = \sigma_{\text{passive elastic}} + \sigma_{\text{active}}$, as Fig. 3a specifically in tensor notation this gives:

$$\sigma_{ij} = \frac{hE}{1+\nu}\left(\epsilon_{ij} + \frac{\nu}{1-\nu}\epsilon_{kk}\delta_{ij}\right) + \frac{hE}{2(1-\nu)}P(\mathbf{x})\delta_{ij},$$

Where we use the summation convention and introduce the kronecker delta. The active contractility is assumed to act isotropically. The deformations are then determined from the force balance

$$\nabla \cdot \sigma - KT(\mathbf{x})\mathbf{u} = \mathbf{0},$$

Where K quantifies substrate resistance to deformation and $T(\mathrm{x})$ is an indicator function that take the value of 1 where the cell is adhered and 0 otherwise. The contractility function is assumed to be constant throughout the layer $P(\mathrm{x})=P_0$, for Fig. 3, with the addition of a monotonic increasing contractility profile $P(\mathrm{x})=a(1+b\mathrm{r}^5)$ for Fig. 4. The polynomial contractility profile is selected to enable analytical phase plane analysis. Where adhesion is uniform analytical solutions of the force balance equation may be obtained by standard techniques as the resulting equations are of Bessel type and solutions may be obtained by variation of parameters. Where non-uniform adhesion is observed numerical solutions of the force balance equation are obtained using finite element methods within the MATLAB PDE Toolbox.

<u>Adhesion geometry</u>

For uniform adhesion the indicator function is either taken as unity throughout for the disk geometry or as unity in the ring region. Where adhesion is informed by the pFAK data (Fig. 1) and modelled as non-uniform we take the resulting adhesion geometry is as in Fig. 1h. Specifically, we consider two thin annuli of thickness r_t=0.06 at the edges of the micropatterned ring corresponding to the regions with highest intensity pFAK. Additionally, we set a distribution of adhered spots in the internal region and between the two annuli as the pFAK intensity is non-zero in these regions; spots between the two annuli have a radius of r_s=0.0167r_0 and in the internal region have radius r_s=0.018r_0. In these adhered regions T(x)=1 and elsewhere we set T(x)=0.

Acknowledgements

We would like to thank the High-throughput screening STP at the Francis Crick Institute, especially Ok-Ryul Song and Michael Howell for sharing the EpH4-Cas9 cells. This work would not have been possible without the support from the CALM STP especially Matt Renshaw, and Making STP especially Ravi Desai and Christina Dix, at the Francis Crick Institute and the bioAFM and bioImaging facilities within FBMH at the University of Manchester. We would like to thank Stefania Marcotti, Richard Thorogood, Nigel Hodson, Olivia Courbot and Alberto Elosegui-Artola for advice on the analysis of AFM data. We would like to thank Guillaume Charras and Alberto Elosegui-Artola for advice on the manuscript. JRD was supported by a Wellcome Trust Sir Henry Wellcome fellowship (201358/Z/16/Z). JSW was supported by postdoctoral EPSRC funding (EP/W522302/1). This work was supported by a Wellcome Trust Investigator award (107885/Z/15/Z) to NT. Work in the Tapon lab is supported by the Francis Crick Institute, which receives its core funding from Cancer Research UK (CC2138), the UK Medical Research Council (CC2138), and the Wellcome Trust (CC2138). For Open Access, the authors have applied a CC BY public copyright licence to any Author Accepted Manuscript version arising from this submission.

752 1. Mao, Y. & Baum, B. Tug of war-The influence of opposing physical forces on epithelial
753 cell morphology. *Dev Biol* **401**, 92–102 (2015).
754 2. Clarke, D. N. & Martin, A. C. Actin-based force generation and cell adhesion in tissue
755 morphogenesis. *Current Biology* **31**, R667–R680 (2021).
756 3. Pandya, P., Orgaz, J. L. & Sanz-Moreno, V. Actomyosin contractility and collective
757 migration: may the force be with you. *Curr Opin Cell Biol* **48**, 87–96 (2017).
758 4. Lim, S. E., Vicente-Munuera, P. & Mao, Y. Forced back into shape: Mechanics of
759 epithelial wound repair. *Curr Opin Cell Biol* **87**, 102324 (2024).
760 5. Gómez-González, M., Latorre, E., Arroyo, M. & Trepat, X. Measuring mechanical
761 stress in living tissues. *Nature Reviews Physics* **2**, 300–317 (2020).
762 6. Lekka, M., Gnanachandran, K., Kubiak, A., Zieliński, T. & Zemła, J. Traction force
763 microscopy – Measuring the forces exerted by cells. *Micron* **150**, (2021).
764 7. Maruthamuthu, V., Sabass, B., Schwarz, U. S. & Gardel, M. L. Cell-ECM traction force
765 modulates endogenous tension at cell-cell contacts. *Proceedings of the National*
766 *Academy of Sciences* **108**, 4708–4713 (2011).
767 8. McCain, M. L., Lee, H., Aratyn-Schaus, Y., Kléber, A. G. & Parker, K. K. Cooperative
768 coupling of cell-matrix and cell-cell adhesions in cardiac muscle. *Proc Natl Acad Sci U*
769 *S A* **109**, 9881–9886 (2012).
770 9. Sim, J. Y. *et al.* Spatial distribution of cell-cell and cell-ECM adhesions regulates force
771 balance while main taining E-cadherin molecular tension in cell pairs. *Mol Biol Cell* **26**,
772 2456–2465 (2015).
773 10. Ng, M. R., Besser, A., Brugge, J. S. & Danuser, G. Mapping the dynamics of force
774 transduction at cell-cell junctions of epithelial clusters. *Elife* **3**, e03282 (2014).
775 11. Trepat, X. *et al.* Physical forces during collective cell migration. *Nat Phys* **5**, 426–430
776 (2009).
777 12. Tambe, D. T. *et al.* Collective cell guidance by cooperative intercellular forces. *Nat*
778 *Mater* **10**, 469–75 (2011).
779 13. Tambe, D. T. *et al.* Monolayer Stress Microscopy: Limitations, Artifacts, and Accuracy
780 of Recovered Intercellular Stresses. *PLoS One* **8**, e55172 (2013).
781 14. Haas, A. J. *et al.* Interplay between Extracellular Matrix Stiffness and JAM-A Regulates
782 Mechanical Load on ZO-1 and Tight Junction Assembly. *Cell Rep* **32**, 107924 (2020).
783 15. Mohan, A. *et al.* Spatial Proliferation of Epithelial Cells Is Regulated by E-Cadherin
784 Force. *Biophys J* **115**, 853–864 (2018).
785 16. Bonnet, I. *et al.* Mechanical state, material properties and continuous description of
786 an epithelial tissue. *J R Soc Interface* **9**, 2614–2623 (2012).
787 17. Bambardekar, K., Clément, R., Blanc, O., Chardès, C. & Lenne, P.-F. Direct laser
788 manipulation reveals the mechanics of cell contacts in vivo. *Proceedings of the*
789 *National Academy of Sciences* **112**, 1416–1421 (2015).
790 18. Goodwin, K. *et al.* Basal Cell-Extracellular Matrix Adhesion Regulates Force
791 Transmission during Tissue Morphogenesis. *Dev Cell* **39**, 611–625 (2016).
792 19. Davis, J. R. *et al.* ECM degradation in the Drosophila abdominal epidermis initiates
793 tissue growth that ceases with rapid cell-cycle exit. *Current Biology* **32**, 1285-1300.e4
794 (2022).
795 20. Sonam, S. *et al.* Mechanical stress driven by rigidity sensing governs epithelial
796 stability. *Nat Phys* **19**, 132–141 (2023).
797 21. Kozyrina, A. N., Piskova, T. & Di Russo, J. Mechanobiology of Epithelia From the
798 Perspective of Extracellular Matrix Heterogeneity. *Front Bioeng Biotechnol* **8**, (2020).

22. Díaz-de-la-Loza, M. del C. & Stramer, B. M. The extracellular matrix in tissue morphogenesis: No longer a backseat driver. *Cells and Development* **177**, 203883 (2024).
23. Diller, R. B. & Tabor, A. J. The Role of the Extracellular Matrix (ECM) in Wound Healing: A Review. *Biomimetics* **7**, 14–16 (2022).
24. Winkler, J., Abisoye-Ogunniyan, A., Metcalf, K. J. & Werb, Z. Concepts of extracellular matrix remodelling in tumour progression and metastasis. *Nat Commun* **11**, 1–19 (2020).
25. Oakes, P. W., Banerjee, S., Marchetti, M. C. & Gardel, M. L. Geometry regulates traction stresses in adherent cells. *Biophys J* **107**, 825–833 (2014).
26. Mertz, A. F. *et al.* Scaling of Traction Forces with the Size of Cohesive Cell Colonies. *Phys Rev Lett* **108**, 198101 (2012).
27. Reichmann, E., Ball, R., Groner, B. & Friis, R. R. New mammary epithelial and fibroblastic cell clones in coculture form structures competent to differentiate functionally. *J Cell Biol* **108**, 1127–1138 (1989).
28. Guvendiren, M. & Burdick, J. A. Stiffening hydrogels to probe short- and long-term cellular responses to dynamic mechanics. *Nat Commun* **3**, 792 (2012).
29. Lopez, J. I., Kang, I., You, W. K., McDonald, D. M. & Weaver, V. M. In situ force mapping of mammary gland transformation. *Integrative Biology* **3**, 910–921 (2011).
30. Teixeira, A. M. & Martins, P. A review of bioengineering techniques applied to breast tissue: Mechanical properties, tissue engineering and finite element analysis. *Frontiers in Bioengineering and Biotechnology* vol. 11 Preprint at https://doi.org/10.3389/fbioe.2023.1161815 (2023).
31. Maschler, S. M. *et al.* Tumor cell invasiveness correlates with changes in integrin expression and localization. *Oncogene* **24**, 2032–2041 (2005).
32. Kwon, M. Y. *et al.* Influence of hyaluronic acid modification on CD44 binding towards the design of hydrogel biomaterials. *Biomaterials* **222**, 119451 (2019).
33. Loebel, C., Mauck, R. L. & Burdick, J. A. Local nascent protein deposition and remodelling guide mesenchymal stromal cell mechanosensing and fate in three-dimensional hydrogels. *Nat Mater* **18**, 883–891 (2019).
34. Loebel, C. *et al.* Metabolic labeling of secreted matrix to investigate cell–material interactions in tissue engineering and mechanobiology. *Nature Protocols* vol. 17 618–648 Preprint at https://doi.org/10.1038/s41596-021-00652-9 (2022).
35. Kechagia, J. Z., Ivaska, J. & Roca-Cusachs, P. Integrins as biomechanical sensors of the microenvironment. *Nat Rev Mol Cell Biol* **20**, 457–473 (2019).
36. Han, S. J., Bielawski, K. S., Ting, L. H., Rodriguez, M. L. & Sniadecki, N. J. Decoupling substrate stiffness, spread area, and micropost density: A close spatial relationship between traction forces and focal adhesions. *Biophys J* **103**, 640–648 (2012).
37. Fusco, S., Panzetta, V. & Netti, P. A. Mechanosensing of substrate stiffness regulates focal adhesions dynamics in cell. *Meccanica* **52**, 3389–3398 (2017).
38. Panzetta, V., Fusco, S. & Netti, P. A. Cell mechanosensing is regulated by substrate strain energy rather than stiffness. *Proc Natl Acad Sci U S A* **116**, 22004–22013 (2019).
39. Han, S. J., Oak, Y., Groisman, A. & Danuser, G. Traction microscopy to identify force modulation in subresolution adhesions. *Nat Methods* **12**, 653–656 (2015).
40. Solowiej-Wedderburn, J. & Dunlop, C. M. Cell-strain-energy costs of active control of contractility. *Phys Rev E* **107**, (2023).

845 41. Banerjee, S. & Marchetti, M. C. Contractile Stresses in Cohesive Cell Layers on Finite-
846 Thickness Substrates. *Phys Rev Lett* **109**, 108101 (2012).
847 42. Ruppel, A. *et al.* Force propagation between epithelial cells depends on active
848 coupling and mechano-structural polarization. *Elife* **12**, 1–42 (2023).
849 43. Alcaraz, J. *et al.* Laminin and biomimetic extracellular elasticity enhance functional
850 differentiation in mammary epithelia. *EMBO Journal* **27**, 2829–2838 (2008).
851 44. Rheinlaender, J. *et al.* Cortical cell stiffness is independent of substrate mechanics.
852 *Nat Mater* **19**, 1019–1025 (2020).
853 45. Doss, B. L. *et al.* Cell response to substrate rigidity is regulated by active and passive
854 cytoskeletal stress. *Proc Natl Acad Sci U S A* **117**, 12817–12825 (2020).
855 46. Valon, L., Marín-Llauradó, A., Wyatt, T., Charras, G. & Trepat, X. Optogenetic control
856 of cellular forces and mechanotransduction. *Nat Commun* **8**, (2017).
857 47. Ayad, N. M. E., Kaushik, S. & Weaver, V. M. Tissue mechanics, an important regulator
858 of development and disease. *Philosophical Transactions of the Royal Society B:*
859 *Biological Sciences* vol. 374 Preprint at https://doi.org/10.1098/rstb.2018.0215
860 (2019).
861 48. De Mets, R. *et al.* Cellular tension encodes local Src-dependent differential β1 and β3
862 integrin mobility. *Mol Biol Cell* **30**, 181–190 (2019).
863 49. Von Erlach, T. C., Hedegaard, M. A. B. & Stevens, M. M. High resolution Raman
864 spectroscopy mapping of stem cell micropatterns. *Analyst* **140**, 1798–1803 (2015).
865 50. Sharrock, T. E. & Sanson, B. Cell sorting and morphogenesis in early Drosophila
866 embryos. *Semin Cell Dev Biol* **107**, 147–160 (2020).
867 51. Munjal, A. & Lecuit, T. Actomyosin networks and tissue morphogenesis. *Development*
868 *(Cambridge)* **141**, 1789–1793 (2014).
869 52. Miao, H. & Blankenship, J. T. The pulse of morphogenesis: Actomyosin dynamics and
870 regulation in epithelia. *Development (Cambridge)* **147**, (2020).
871 53. Krishnan, R. *et al.* Substrate stiffening promotes endothelial monolayer disruption
872 through enhanced physical forces. *Am J Physiol Cell Physiol* **300**, 146–154 (2011).
873 54. Mertz, A. F. *et al.* Cadherin-based intercellular adhesions organize epithelial cell-
874 matrix traction forces. *Proc Natl Acad Sci U S A* **110**, 842–847 (2013).
875 55. Pérez-González, C. *et al.* Active wetting of epithelial tissues. *Nat Phys* **15**, 79–88
876 (2019).
877 56. Palmquist, K. H. *et al.* Reciprocal cell-ECM dynamics generate supracellular fluidity
878 underlying spontaneous follicle patterning. *Cell* **185**, 1960-1973.e11 (2022).
879 57. Trichet, L. *et al.* Evidence of a large-scale mechanosensing mechanism for cellular
880 adaptation to substrate stiffness. *Proc Natl Acad Sci U S A* **109**, 6933–8 (2012).
881 58. Nier, V. *et al.* Inference of Internal Stress in a Cell Monolayer. *Biophys J* **110**, 1625–
882 1635 (2016).
883 59. Chen, T., Saw, T. B., Mege, R. M. & Ladoux, B. Mechanical forces in cell monolayers. *J*
884 *Cell Sci* **131**, (2018).
885 60. Yamada, S. & Nelson, W. J. Localized zones of Rho and Rac activities drive initiation
886 and expansion of epithelial cell-cell adhesion. *Journal of Cell Biology* **178**, 517–527
887 (2007).
888 61. Solowiej-Wedderburn, J. & Dunlop, C. M. Sticking around: Cell adhesion patterning
889 for energy minimization and substrate mechanosensing. *Biophys J* **121**, 1777–1786
890 (2022).

62. Edwards, C. M. & Schwarz, U. S. Force localization in contracting cell layers. *Phys Rev Lett* **107**, 1–5 (2011).
63. Prost, J., Jülicher, F. & Joanny, J. F. Active gel physics. *Nat Phys* **11**, 111–117 (2015).

Figure 1

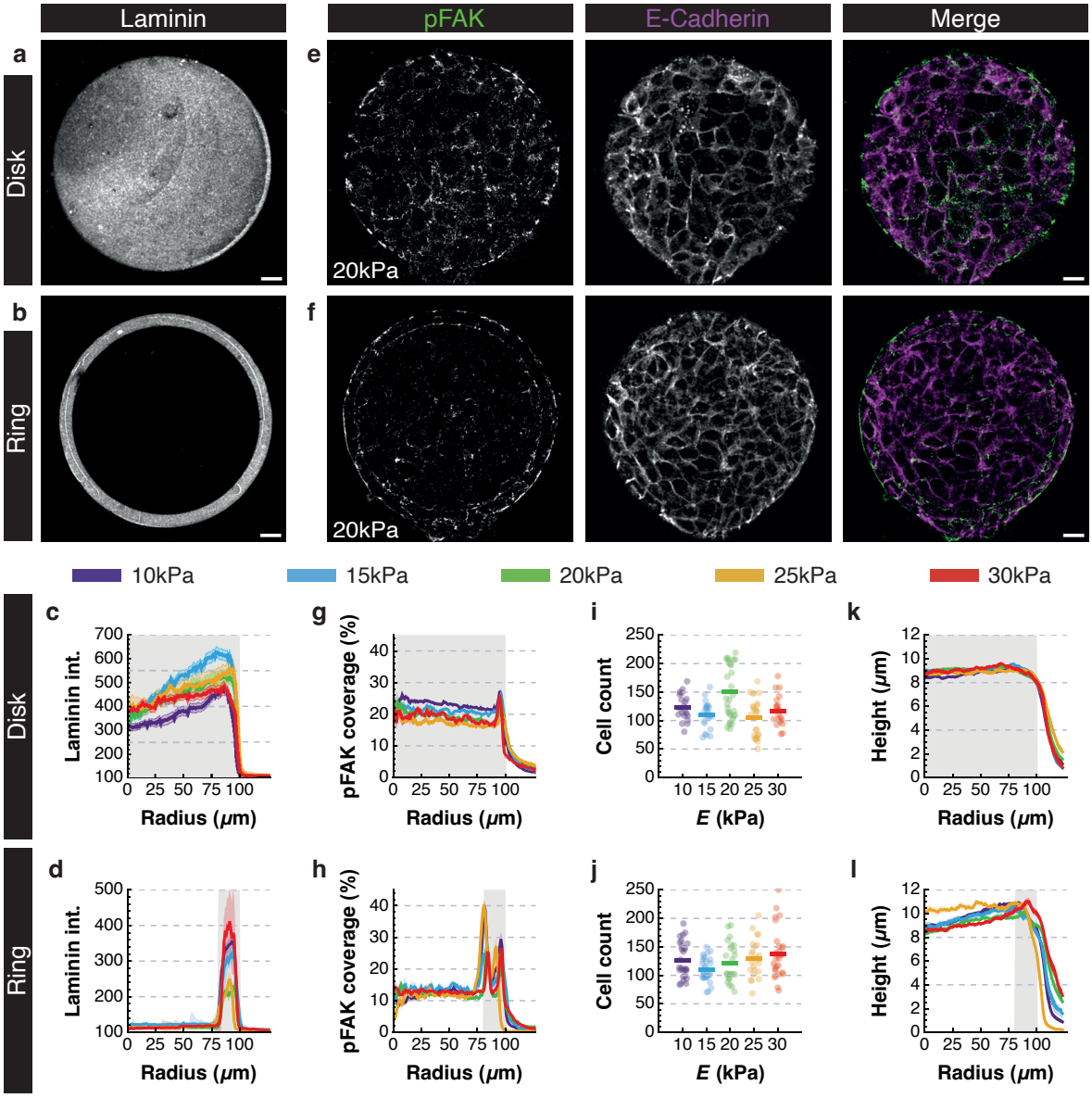
Laminin
pFAK
E-Cadherin
Merge
a
b
e
f
Disk
Ring
20kPa
20kPa
10kPa
15kPa
20kPa
25kPa
30kPa
c
d
g
h
i
j
k
l
Laminin int.
pFAK coverage (%)
Cell count
Height (μm)
Radius (μm)
E (kPa)

896 **Fig. 1. Modulating adhesive surface of EpH4 monolayers. a,b** Example projection of laminin
897 micropatterns for disk (**a**) and ring (**b**). **c,d** Quantification of mean laminin intensity radially
898 across micropatterns. **e,f** Example projections of basal pFAK and apical E-Cadherin on disk
899 (**e**) and ring (**f**) micropatterns. **g,h** Quantification of mean pFAK coverage radially across
900 micropatterns. **i,j** Dot plot of cell number within each monolayer, bars highlight mean value
901 for each population. **k,l** Quantification of mean cell height radially across micropatterns.
902 Scale bars = 20μm. For all quantification thick line are mean values and ribbons are S.E.M,
903 grey shaded region represents adhesive surface. All N numbers and statistics included in
904 statistical Table.
905
906
907

Figure 2

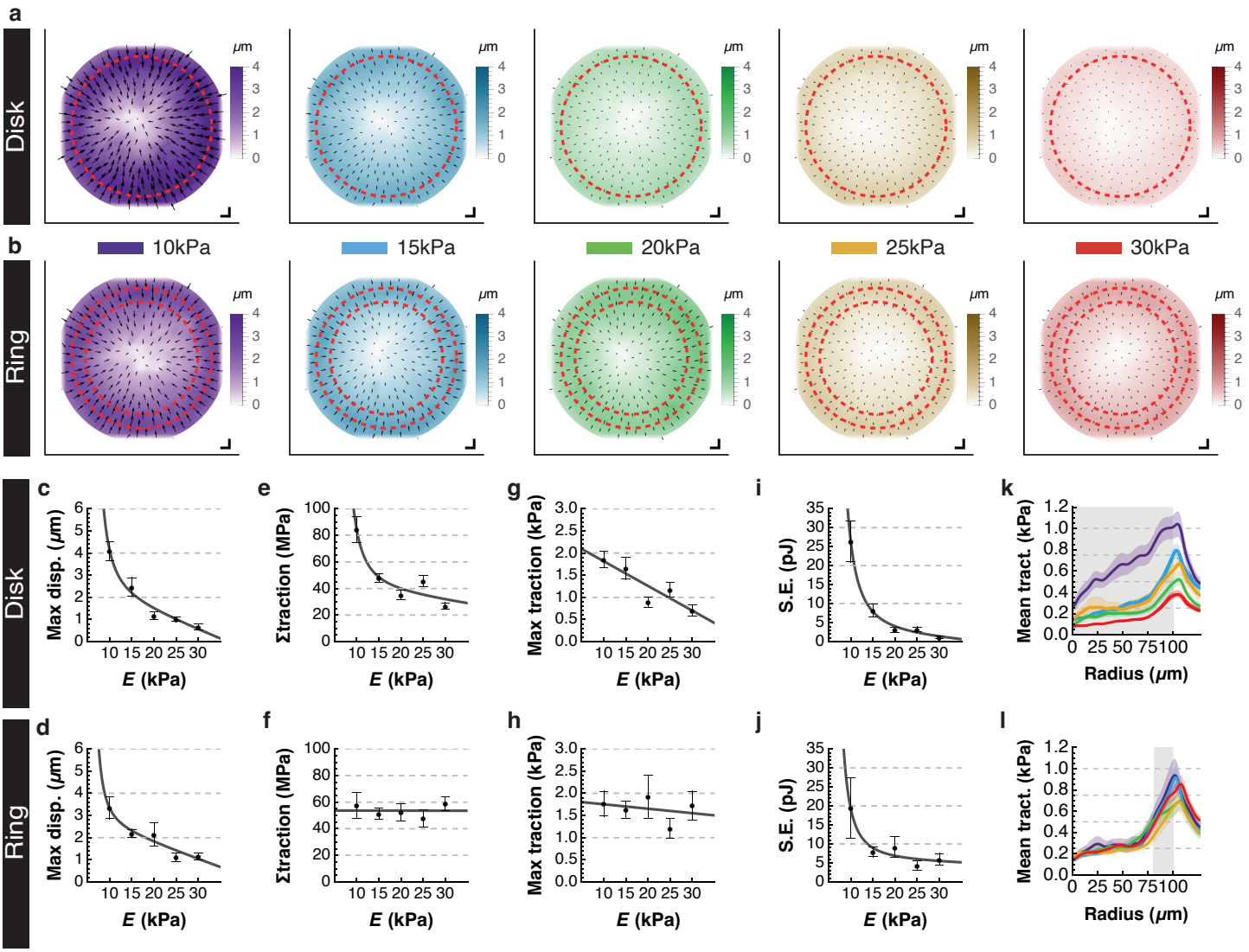
a
Disk
b
Ring
10kPa
15kPa
20kPa
25kPa
30kPa
μm
c
d
e
f
g
h
i
j
k
l
Max disp. (μm)
Σtraction (MPa)
Max traction (kPa)
S.E. (pJ)
Mean tract. (kPa)
E (kPa)
Radius (μm)

Fig. 2. Monolayer traction stresses are altered by modulating adhesive surface. a,b Mean displacement vector plots for monolayers on disks (**a**) and rings (**b**) on different substrate stiffnesses. Red dashed line outlines the adhesive surface and scale bars represent 4μm. **c,d** Quantification of maximum bead displacement by monolayers adhered to disks and rings on different substrate stiffnesses. **e,f** Quantification of total traction forces generated by monolayers adhered to disks and rings on different substrate stiffnesses. **g,h** Quantification of maximum traction forces generated by monolayers adhered to disks and rings on different substrate stiffnesses. **i,j** Quantification of strain energy transferred by monolayers into substrate adhered to disks and rings on different substrate stiffnesses. For **c-j** black dots highlight mean value, whiskers represent S.E.M and grey line is line of best fit. **k,l** Quantification of mean traction forces radially across micropatterns. Thick lines are mean values and ribbons are S.E.M, grey shaded region represents adhesive surface.

Figure 3

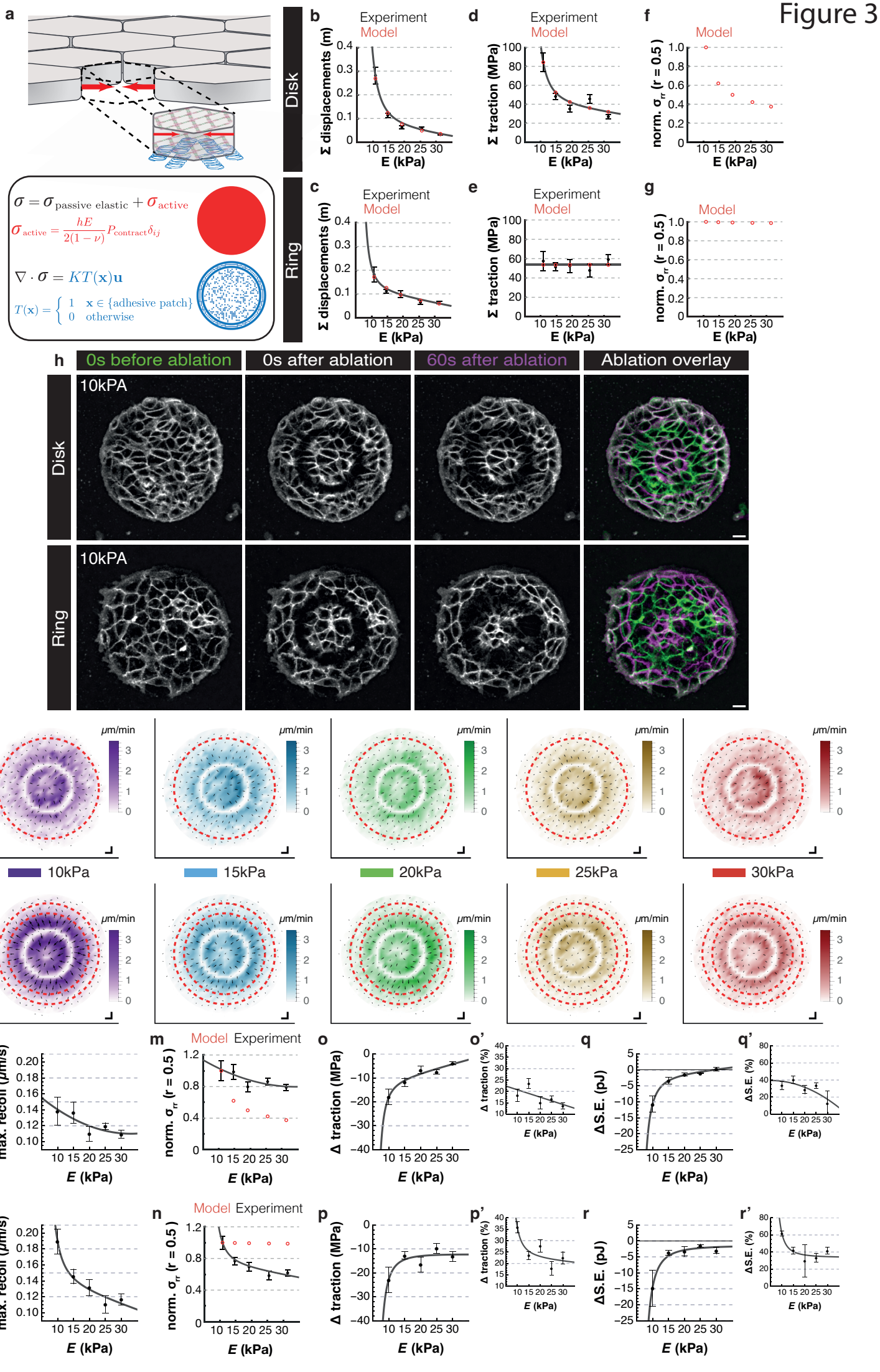
a
$\sigma = \sigma_{\text{passive elastic}} + \sigma_{\text{active}}$
$\sigma_{\text{active}} = \frac{hE}{2(1-\nu)} P_{\text{contract}} \delta_{ij}$
$\nabla \cdot \sigma = KT(\mathbf{x})\mathbf{u}$
$T(\mathbf{x}) = \begin{cases} 1 & \mathbf{x} \in \{\text{adhesive patch}\} \\ 0 & \text{otherwise} \end{cases}$
Disk
Ring
b
c
d
e
f
g
Experiment
Model
Σ displacements (m)
Σ traction (MPa)
norm. σ_{rr} (r = 0.5)
E (kPa)
h
0s before ablation
0s after ablation
60s after ablation
Ablation overlay
10kPA
i
j
μm/min
10kPa
15kPa
20kPa
25kPa
30kPa
k
l
m
n
o
p
o'
p'
q
r
q'
r'
max. recoil (μm/s)
Δ traction (%)
ΔS.E. (pJ)
ΔS.E. (%)
E (kPa)

Fig. 3. Intercellular stress is not proportional to traction stress. a Schematic representation of the major components that comprise the force balance model. Cells are considered as active contractile agents (red arrows) bound together to form a monolayer continuum as well as being bound to the substrate through adhesions (blue springs). Any stresses within the monolayer are therefore a product of these active forces and passive elastic forces transmitted through the monolayer (top equation). The active forces generated by the cells are modelled as a pressure term (red equation) describing cell contractility, and for the initial model we assumed a uniform distribution of contractility. Cell adhesions are distributed throughout the monolayer based on experimental observations (blue schematic), and at these points stresses within the monolayer are transmitted to the substrate to deform it (bottom two equations). Schematic produced in part with Biorender.com. **b,c** Total hydrogel displacement from experiments (same as Extended data Fig. 2g,h) were used to parameterise the model. **d,e** Based on this parameterisation the model is able to recapitulate the overall trend in experimental traction forces (same as Fig. 2e,f). **f,g** Model predictions on intercellular stresses at the radial midpoint of the layer (r=0.5) normalised to E=10kPa show changes as substrate stiffness increases. The model predicts intercellular forces change in a manner similar to the total traction forces as substrate stiffness increases. **h** Example time course projections of our laser ablation procedure for both micropatterns. A ring ROI with outer radius of 50µm and inner radius of 40µm was ablated. Merge shows overlay of 0s before and 60s after the ablation only to highlight deformations, where white highlights regions of no deformation. Scale bar = 20µm. **i,j** Mean recoil velocity vector plots for monolayers on disks (**i**) and rings (**j**) on different substrate stiffnesses. Red dashed line outlines the adhesive surface and scale bars represent 3.5µm/min. **k,l** Quantification of maximum recoil velocity after ablation for monolayers adhered to disks and rings on different substrate stiffnesses. **m,n** Recoil velocity (same as Fig. 3k,l) and model predictions of radial midpoint intercellular stresses (same as Fig. 3f,g) where both have been normalised to the value on the softest hydrogel (E=10kPa). The model is not able to mimic experimental observations. **o,p** Quantification of the total loss in traction forces once a new steady state is reached after ablations for monolayers adhered to disks and rings on different substrate stiffnesses. Where **o',p'** represent this value as a percentage of total traction forces (see Fig. 2e,f). **q,r** Quantification of the total loss in strain energy once a new steady state is reached after ablations for monolayers

adhered to disks and rings on different substrate stiffnesses. Where **q',r'** represent this value as a percentage of total strain energy (see Fig. 2i,j). For all quantification graphs, experimental data is in black, with dots representing mean value, whiskers the S.E.M and grey line the line of best fit. Model outputs are red circles, where included.

Figure 4

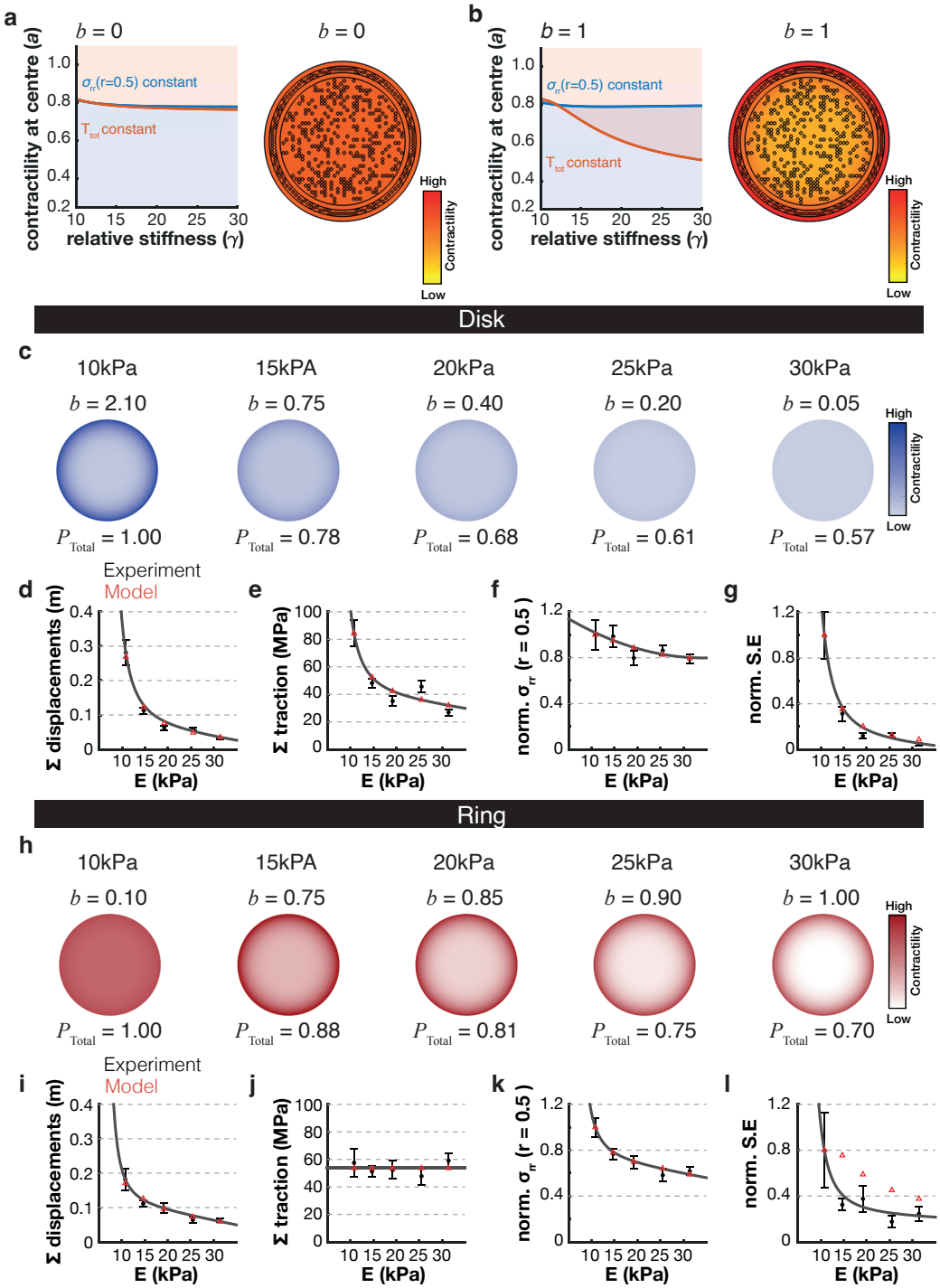
a
b = 0
b = 0
contractility at centre (a)
σrr(r=0.5) constant
Ttot constant
relative stiffness (γ)
High
Contractility
Low
b
b = 1
b = 1
contractility at centre (a)
σrr(r=0.5) constant
Ttot constant
relative stiffness (γ)
High
Contractility
Low
Disk
c
10kPa
15kPA
20kPa
25kPa
30kPa
b = 2.10
b = 0.75
b = 0.40
b = 0.20
b = 0.05
High
Contractility
Low
PTotal = 1.00
PTotal = 0.78
PTotal = 0.68
PTotal = 0.61
PTotal = 0.57
d
Experiment
Model
Σ displacements (m)
E (kPa)
e
Σ traction (MPa)
E (kPa)
f
norm. σrr (r = 0.5)
E (kPa)
g
norm. S.E
E (kPa)
Ring
h
10kPa
15kPA
20kPa
25kPa
30kPa
b = 0.10
b = 0.75
b = 0.85
b = 0.90
b = 1.00
High
Contractility
Low
PTotal = 1.00
PTotal = 0.88
PTotal = 0.81
PTotal = 0.75
PTotal = 0.70
i
Experiment
Model
Σ displacements (m)
E (kPa)
j
Σ traction (MPa)
E (kPa)
k
norm. σrr (r = 0.5)
E (kPa)
l
norm. S.E
E (kPa)

Fig. 4. Non-uniform contractility reconciles experimental observations. a,b Phase plane plots of contractility in the centre of the monolayer against substrate stiffness for ring monolayers only. The examples showcase situations where the spatial distribution of contractility (b), represented with accompanying heatmaps, is either uniform (b =0, **a**) or non-uniform (b =1, **b**). In both, solid lines represent situations where either intercellular stress at the radial midpoint of the layer (r=0.5) is constant (blue lines) or total traction forces generated by the monolayer is constant (red line). The shaded regions represent either situations where the intercellular stress must be lower (blue shaded region) or total traction forces must be greater (red shaded area). Note on uniform contractility there is no workable overlap of shaded regions meaning no workable parameters exist that allow constant traction forces but lower intercellular stresses as substrate stiffness increases as occurs experimentally, however with non-uniform contractility an overlap region does exist highlighting a large parameter space which could reconcile experimental observations. For **c-l** the model was parameterised to include non-uniform contractility for both disks (**c-g**) and rings (**h-l**). **c,h** Schematic representations of the total and spatial distribution of contractility parameters (b = spatial distribution of contractility; P = total contractility normalised to softest substrate) used for disk (**c**) and rings (**h**) on different substrate stiffnesses. **d,i** Total hydrogel displacement from experiments (same as Extended data Fig. 2g,h), **e,j** total traction forces (same as Fig. 2e,f), and **f,k** normalised intercellular stress at the radial midpoint of the layer (r=0.5) normalised to the softest substrate (same as Fig. 3m,n) were used to parameterise the model. **g,l** Normalised strain energy to the softest substrate was used as a final check to examine the power of the model to mimic all experimental observations. Note that for disks (**g**) the model can reproducibly mimic experimental observations but for rings (**l**) it mimics the trend but not reproduce the actual change. The discrepancy may be due to non-local effects from the thickness of the hydrogel not being fully accounted for in the model. For all quantification graphs, experimental data is in black, with dots representing mean value, whiskers the S.E.M and grey line the line of best fit and model outputs are red triangles.

Figure 5

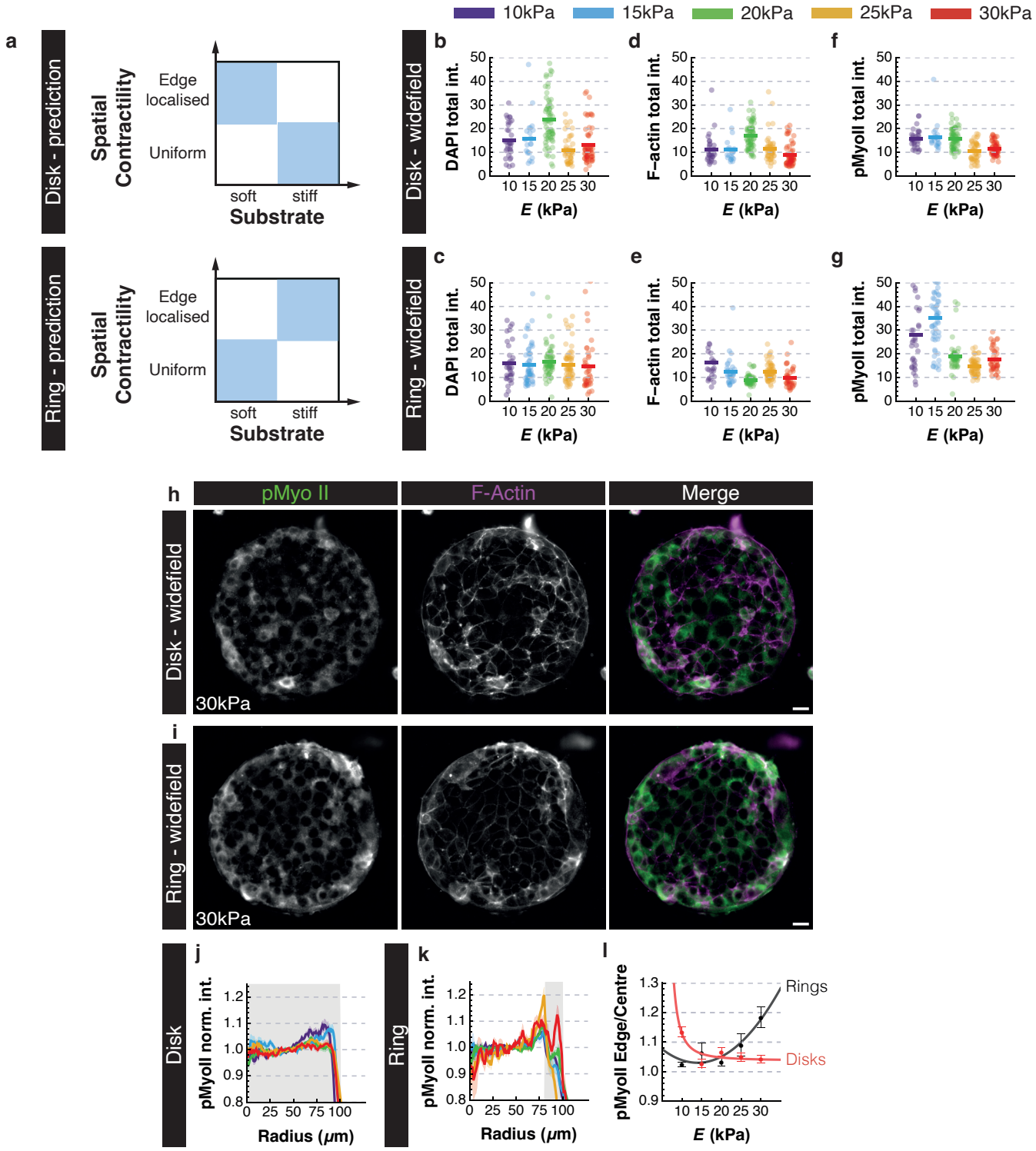
10kPa
15kPa
20kPa
25kPa
30kPa
a
Disk - prediction
Spatial Contractility
Edge localised
Uniform
soft
stiff
Substrate
Ring - prediction
Disk - widefield
Ring - widefield
b
c
d
e
f
g
DAPI total int.
F-actin total int.
pMyoII total int.
E (kPa)
h
i
pMyo II
F-Actin
Merge
30kPa
Disk
Ring
j
k
l
pMyoII norm. int.
Radius (μm)
pMyoII Edge/Centre
Rings
Disks

Fig. 5. Contractility is non-uniform across micropatterned monolayers. a Schematic representation of predictions based on parameterisation of the model. For disks the model suggests that there needs to be a shift from contractility focused to the edge on soft substrates to more uniformity on stiffer substrates. On rings, the model suggests the opposite needs to occur with contractility being more uniform on soft substrates and becoming more localised to the edge on stiff substrates. **b-g** Dot plots of total intensity within each monolayer for DAPI (**b,c**), F-actin (**d,e**) and pMyoII (**f,g**) adhered to disks (**b,d,f**) and rings (**c,e,g**). Each dot represents one monolayer, and the bars represent mean value for each population. **h,i** Example images of pMyoII and F-actin on disk (**h**) and ring (**i**) micropatterns. Scale bar = 20µm. **j,k** Quantification of mean normalised pMyoII intensity radially across micropatterns for a basal projection, with the normalisation to the mean intensity at the ablation site (40-50µm). **l** Quantification of edge to centre normalised intensity ratio for pMyoII. Dots represent mean value, whiskers S.E.M and shaded line the line of best fit, with disks in red and rings in black. Note that the trend corroborates the model predictions (**a**).

Extended Data Figure 1

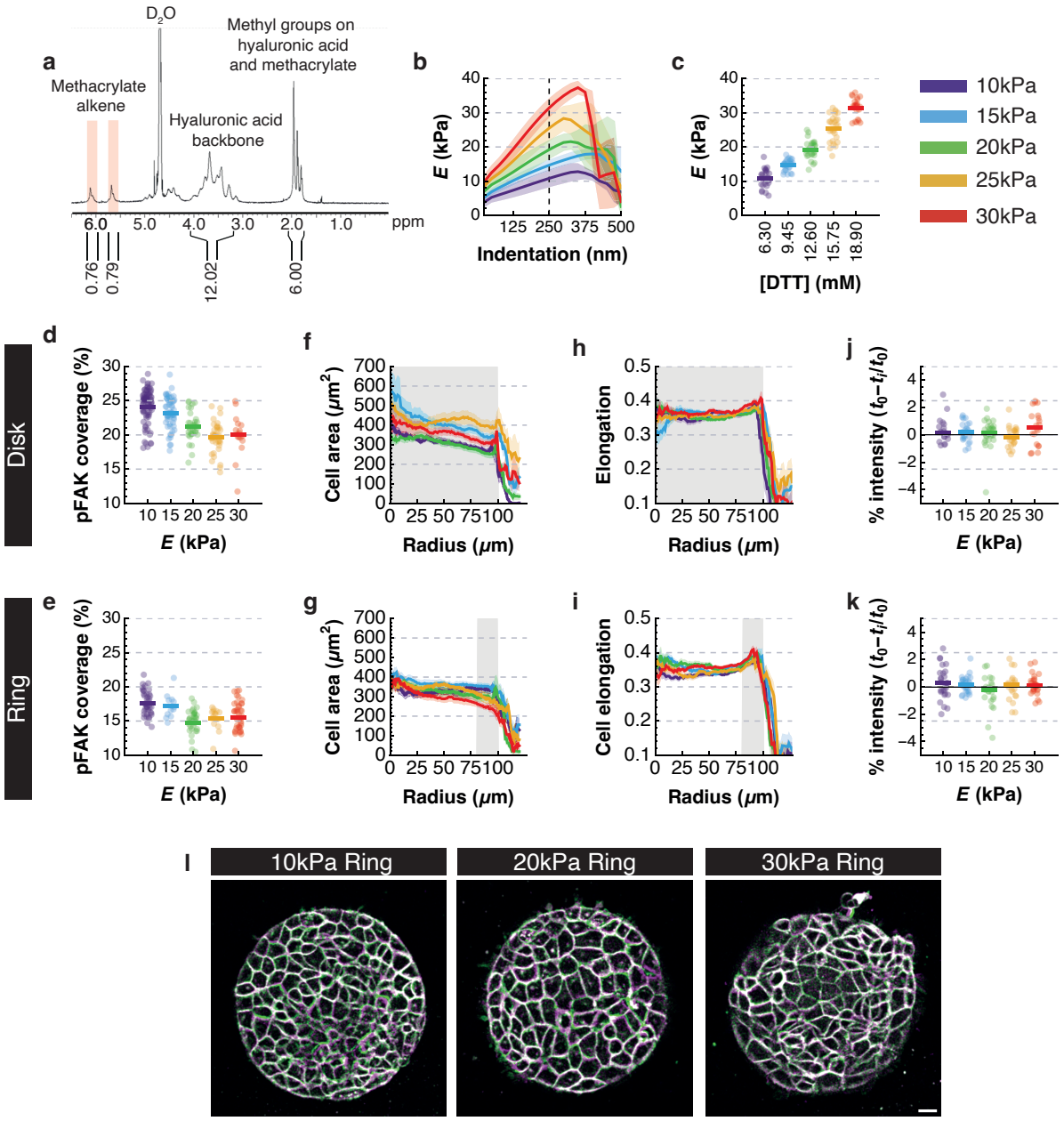

1007 **Extended data Fig. 1. Characterisation of micropatterned MeHA on EpH4 cells. a** ^{1}H NMR
1008 spectra of methacrylated hyaluronic acid (MeHA). **b** Young's moduli at different indentation
1009 depths on 3%(w/v) MeHA hydrogels cross-linked with different DTT concentrations. Dashed
1010 line is at 250nm which was used to define the young's moduli for each DTT concentration. **c**
1011 Dot plot of Young's moduli for each concentration of DTT. Each dot is the average value
1012 from 50 force-curves taken for a 100μm x 100μm region. **d,e** Dot plot of total pFAK
1013 coverage within each monolayer, bars highlight mean value for each population. **f,g**
1014 Quantification of mean cell area radially across micropatterns. **h,i** Quantification of mean
1015 cell elongation radially across micropatterns. For **f-i** thick line are mean values and ribbons
1016 are S.E.M, grey shaded region represents adhesive surface. **j,k** Dot plot of % intensity
1017 change after subtracting the cell outline projection from the frame before an annular
1018 ablation from the initial frame 1 minute before. Lines represent mean value for each
1019 population. **l** Cell outline projections five minutes apart overlayed with the initial frame in
1020 green and last frame in Magenta. White represents pixels where there is no change in
1021 intensity. Scale bar = 20μm.
1022
1023

Extended Data Figure 2

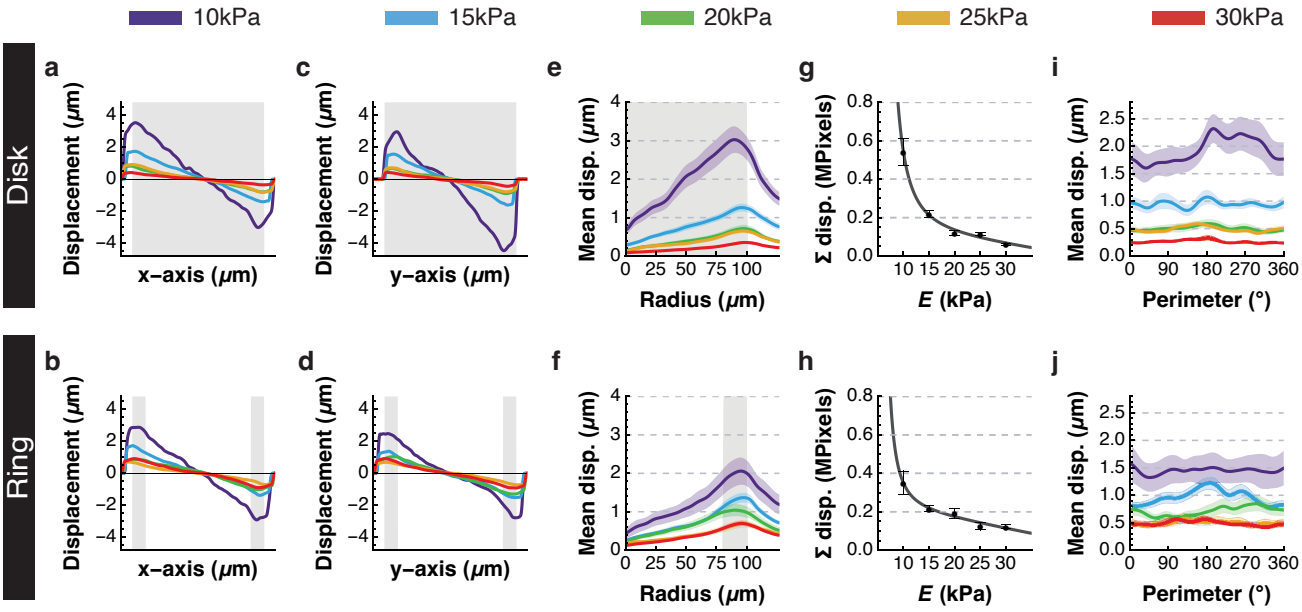

Extended data Fig. 2. Displacements of microbeads embedded within MeHA hydrogels by EpH4 monolayers. a-d Quantification of mean displacement along the x-axis (**a,b**) and y-axis (**c,d**). Grey region represents adhesive surface. **e,f** Quantification of mean displacement radially across micropatterns, where thick lines are mean values, ribbons are S.E.M, and grey shaded region represents adhesive surface. **g,h** Quantification of total bead displacements generated by monolayers adhered to disks and rings on different substrate stiffnesses. Dots represent mean values, whiskers are S.E.M, and grey line is line of best fit. **i,j** Quantification of the mean bead displacement around the perimeter of monolayers, with 0° along the horizontal axis, where thick lines are mean values, ribbons are S.E.M, and grey shaded region represents adhesive surface.

Extended Data Figure 3

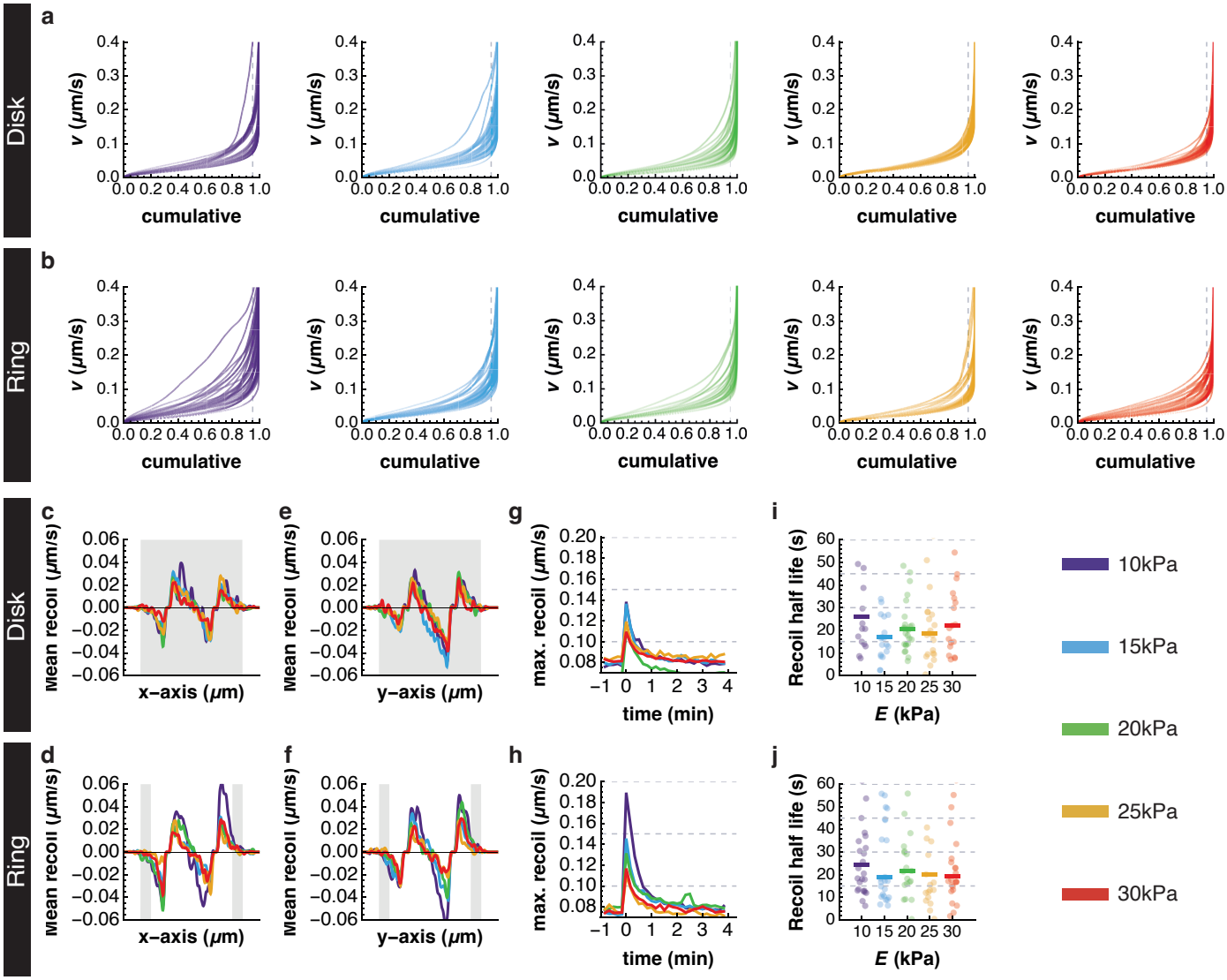

1036 **Extended data Fig. 3. Recoil velocity dynamics and correlations after laser ablation. a,b**
1037 Cumulative plots of all recoil velocity values for each movie on both micropatterns. To
1038 calculate the maximum recoil value the 95th percentile (grey dashed line) value was used,
1039 which was always located near the edge of the ablation site. **c-f** Quantification of mean
1040 recoil velocity along the x-axis (**c,d**) and y-axis (**e,f**). Grey region represents adhesive surface.
1041 **g,h** Quantification of the mean maximum recoil velocity over the time course of our movies
1042 for both micropatterns. **i,j** Dot plot of recoil half-life calculated from Extended data Fig. 3g,h.
1043 Each dot represents a movie, and the line represents population mean value.
1044
1045

Extended Data Figure 4

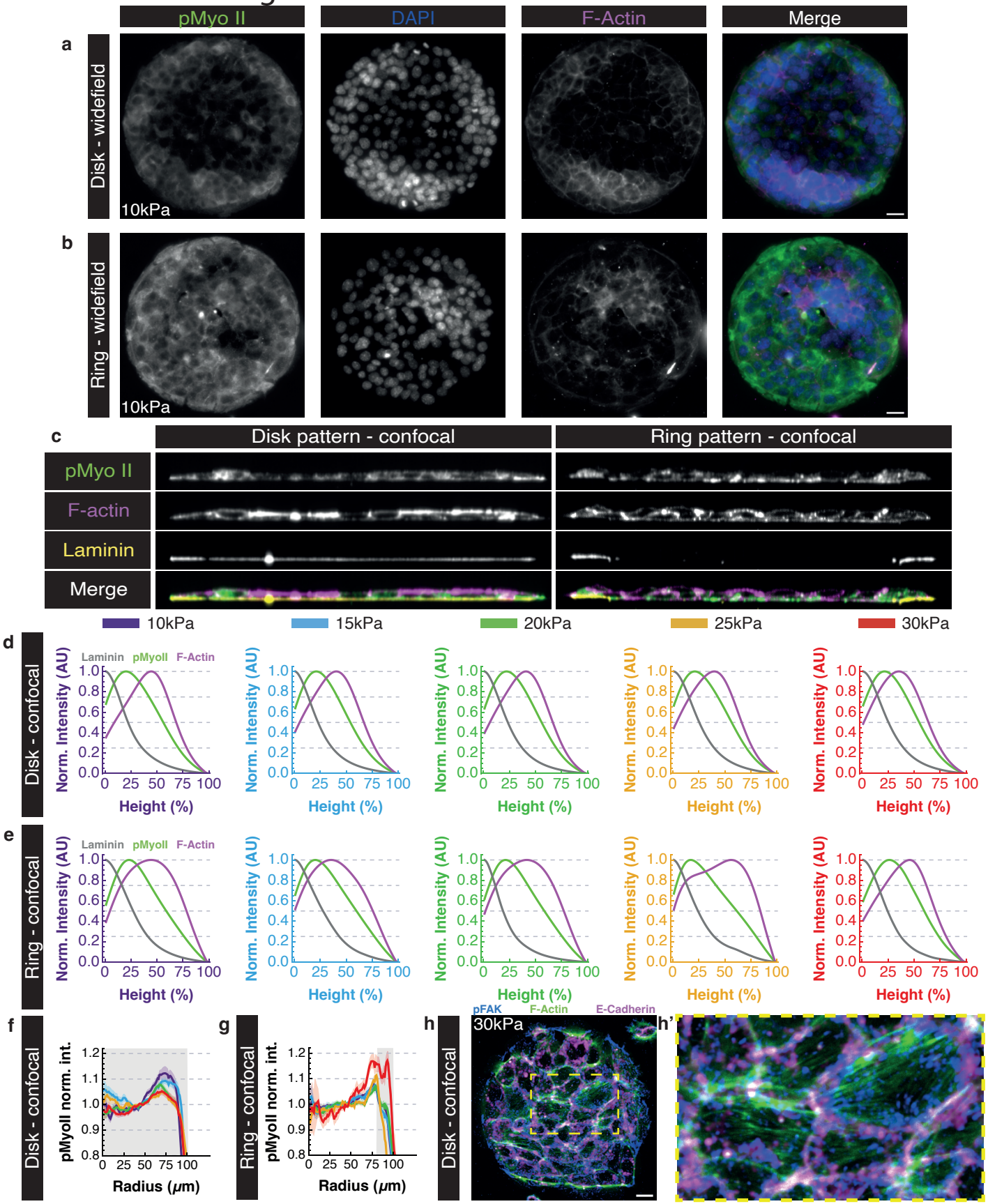

1046 **Extended data Fig. 4. pMyoII localisation within monolayers. a,b** Example images of
1047 pMyoII, DAPI and F-actin on disk (**a**) and ring (**b**) micropatterns. Scale bar = 20μm. **c** Example
1048 orthogonal projections through the middle of a monolayer of pMyoII, F-actin and Laminin
1049 on disk (left) and ring (right) micropatterns. **d,e** Quantification of mean orthogonal intensity
1050 of laminin, pMyoII and F-actin normalised to the maximum value for the entire orthogonal
1051 projection (see **c**). Note that pMyoII maximum intensity is always near the laminin intensity
1052 highlighting basal accumulation of pMyoII. **f,g** Quantification of mean normalised pMyoII
1053 intensity radially across micropatterns for a whole z-projection of the monolayer, with the
1054 normalisation to the mean intensity at the ablation site (40-50μm). Thick line are mean
1055 values, ribbons are S.E.M, and grey shaded region represents adhesive surface. **h** Example
1056 basal projection of pFAK, F-Actin and E-Cadherin on disk micropattern with expanded insert
1057 (**h'**) to highlight F-actin fibres that span epithelial cells, mainly between pFAK labelled
1058 adhesions. Scale bar = 20μm.

Supplementary Information: Monolayer force generation and transmission is dictated by focal adhesion distribution

John Robert Davis, Josephine Solowiej-Wedderburn, Sebastián Vega, Jason Burdick, Carina Dunlop, Nicolas Tapon

Active stress model for confluent cell layers

The active stress model for the cell layer is based on a continuum description with active stress incorporated into the constitutive relations. This is a widely adopted approach, for a detailed treatment see e.g. [1, 2]. Here, due to the relative thinness of the cell layer compared with its extent, and the lack of cell rearrangements (see Extended Data Fig. 1(l)), we assume plane stress and a (linear) elastic response. We additionally assume that the within layer contractility has no preferred direction (isotropic contraction), to give the constitutive relations

$$\sigma_{ij} = \frac{hE}{1+\nu}\left(\epsilon_{ij} + \frac{\nu}{1-\nu}\epsilon_{kk}\delta_{ij}\right) + \frac{hE}{2(1-\nu)}P(\mathbf{x})\delta_{ij}, \tag{1}$$

where E is the Young's modulus of the cells, ν the Poisson's ratio of the cells, and h the thickness of the layer. The function $P(\mathbf{x})$ describes the contractility throughout the cell layer and we initially assume a uniform contractility throughout so that $P(\mathbf{x}) = P_0$. Later where we consider non-uniform contractility, we require a contractility function P such that being closer to the edge of the layer means greater contractile activity. In this case, we follow [3, 4] and use the functional form $P(r) = a(1 + br^5)$. Although any monotonic increasing function would be sufficient [3], a polynomial form has the added benefit that in circular geometries (as considered here) explicit analytical solutions may be obtained. The degree $n = 5$ is chosen to ensure a sufficiently sharp transition from the edge region into centre where there is a more uniform contractile activity. The parameter a is a scaling parameter for the total contractility of the layer. The parameter b represents the extent of the localisation of that contractility to the edge of the layer. See Fig. 1 for some example radial profiles of differential contractility for different parameters a and b.

The model is completed through a force balance equation. Here, we follow [1], and take

$$\nabla \cdot \sigma - KT(\mathbf{x})\mathbf{u} = \mathbf{0}, \tag{2}$$

where $T(\mathbf{x})$ is an indicator function that denotes discrete regions of adhesion so that $T(\mathbf{x}) = 1$ where the layer is adhered and $T(\mathbf{x}) = 0$ where there is no adhesion. The boundary conditions are zero stress on the outer boundary and continuity of both stress and deformation at all internal boundaries. The substrate resistance to deformation has been approximated as linear in the deformations (as if it were comprised of a dense network of linear springs). This approximation becomes exact for thin or stiff gels where deformations become localised, see e.g. the papers [2, 5]. The parameter K thus quantifies the stiffness of the substrate and its resistance to deformation.

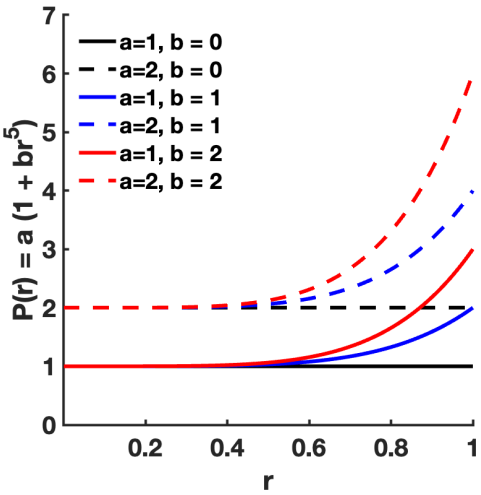

Figure 1: Sketch of differential contractility $P(r) = a(1 + br^5)$. Underlying contractility a is taken as 1 (solid lines) or 2 (dashed lines) each illustrating the effect of varying localisation factors b.

Fixing model parameters

In the constitutive relation (1) we take the parameters as per Table 1. The key control parameter determining model solutions is the non-dimensional parameter $\gamma^2 = K(1-\nu^2)r_0^2/hE$, [1, 4], which quantifies the relative stiffness of substrate and cell layer. The other key element is the contractility function P. K describes the stiffness of the substrate and for very thin substrates it can be shown analytically that this parameter is proportional to Young's modulus of the gel E_s, i.e. $K = \kappa E_s$ [2]. We make this approximation for the substrates used here, validating the approximation from the traction force data. Specifically, for complete adhesion we see that integrating the force balance over the domain A and applying the boundary conditions gives $K = \int_A \nabla \cdot \sigma \mathrm{d}A / \int_A \mathbf{u} \mathrm{d}A$. In Fig. 2, we plot the data from the disc traction force measurements $K = \Sigma T / \Sigma u$ against the gel stiffness E_s. We observe an approximately linear relationship validating the approximation. Taking the mean ratio of K/E_s from all the traction force data gave κ as per Table 1. Finally where the contractility is constant so that $P = P_0$, P_0 may be fitted to either the strain energy or traction data collected from the traction force measurements, and we select traction throughout, see below.

Computational domains

The experiments are performed on two adhesion patterns: a completely functionalised disk (radius 100μm) and a functionalised annular ring with inner and outer radii, 80μm and 100μm, respectively. For the disk we assume complete adhesion so that $T(\mathbf{x}) \equiv 1$ across the whole domain $|\mathbf{r}|/r_0 < 1$. For the ring of outer radius 100μm and inner radius 80μm we consider two patterns of adhesion. For the phase plane analysis, see the main paper Figures 4(a) and 4(b), we consider the ideal arrangement of $T(\mathbf{x}) \equiv 1$ in $0.8 < |\mathbf{r}|/r_0 < 1$, taking advantage of the analytical solutions this symmetry affords (see below). For all other simulations we consider a pattern of adhesion informed by the experimental pFAK imaging data (see e.g. main paper Fig. 1(h)). Specifically, we consider two thin annuli of thickness $r_t = 0.06$ with $T(\mathbf{x}) \equiv 1$ in $0.8 < |\mathbf{r}|/r_0 < 0.8 + r_t$ and $1 - r_t < |\mathbf{r}|/r_0 < 1$, corresponding to the regions with highest intensity pFAK. Additionally, we set a distribution of adhered spots in

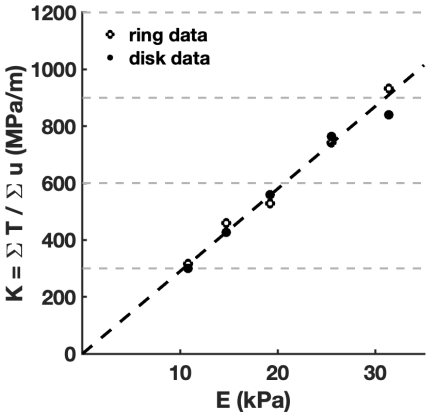

Figure 2: Traction to deformation ratio scales linearly with gel stiffness. Plot shows the ratio of the sum of tractions over the sum of displacements as derived from the experimental data plotted against Young's modulus (E). The dashed line has slope κ, as per Table 1, the mean ratio from all experimental data.

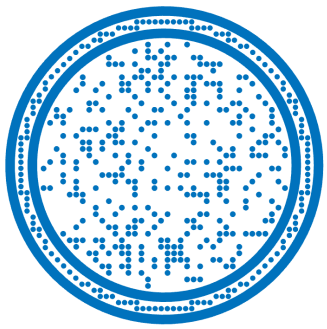

Figure 3: Computational adhesion pattern for simulations of adhesive rings.

Parameter	Value	Source
Young's modulus: cell E	1kPa	literature see e.g. [6]
Layer thickness h	9μm	measured (Fig. 1 k and l in the main paper)
Poisson's ratio: cell ν	0.45	within literature range: 0.38–0.5 [7, 8]
Domain size: radius r_0	100μm	adhesive pattern size
Substrate parameter: κ	29000m^{-1}	estimated from traction data

Table 1: Constitutive parameter values used to calculate dimensionless parameter $\gamma^2 = K(1-\nu^2)r_0^2/hE$ which is used to quantify the relative stiffness of the substrate to the monolayer throughout the study.

the internal region and between the two annuli as the pFAK intensity is non-zero in these regions; spots between the two annuli have a radius of $r_s = 0.0167$ and in the internal region have radius $r_s = 0.018$. The pattern of spot placement used throughout is shown in Fig. 3.

Sensitivity analysis of adhesion patterning

To explore how sensitive the results are to the precise patterning of adhesion, and the possible role of imperfect adhesion in functionalised patches, we simulated different adhesive patterns and looked at their effect on the reported quantities of total traction and internal radial stress at ablation point. For the disk we compared the completely adhered disk used in the study to a simulation with discrete adhesions randomly distributed across the disk, as per Fig. 4A. Specifically, a square grid was generated across the disk such that there were 50 grid squares across the diameter. Adhesions with radius $0.0179r_0$ were then placed in randomly selected grid squares such that the total covered area is approximately 30% the total area of the disk. On this domain, solving on the random domain for the deformations with $\gamma = 15$ and uniform contractility, we calculate the total traction to be $\approx 93\%$ of the total traction calculated with complete adhesion across the entire interface. With the same parameters, we observed similarly small changes in the radial stress at ablation ($\sigma_{rr}(r = 0.5r_0)$): we calculate the $\sigma_{rr}(r = 0.5r_0)$ on the random domain to be $\approx 97\%$ of $\sigma_{rr}(r = 0.5r_0)$ of a disk with complete adhesion.

We further compare different adhesion patterns for the annular micropatterns. The annular micropattern is engineered to cover a region 80μm$< r <$ 100μm such that rings have a width of 20μm; this could be idealised to an adhesion arrangement with $T(\mathbf{x}) \equiv 1$ in $0.8 < |\mathbf{r}|/r_0 < 1$ (Fig. 4B). In table 2 we show that for such ideal arrangements a $\pm 10\mu$m change in internal radius of the disk makes at most a 3% difference to the total traction measured across the layer and similarly small (4%) differences to the radial stress at the point of ablation. Indeed, even with a reduction in adhered area to $r_1 = 0.95$ we see a $\leq 10\%$ change in the total traction and radial stress. For smaller adhered areas we begin to see a sharper drop in the model predicted total traction and radial stress (see e.g. $r_1 = 0.975$ in table 2). As the arrangement of adhesion throughout the cell layer is non-uniform, we also consider different adhesion patterns inspired by the pFAK coverage (see main

paper Fig. 1(j)). Specifically, we considered adhesion patterns with two thin annuli width r_t such that $T(\mathbf{x}) \equiv 1$ in $0.8 < |\mathbf{r}|/r_0 < 0.8 + r_t$ and $1 - r_t < |\mathbf{r}|/r_0 < 1$ (as in Fig. 4C) to represent the regions of higher intensity pFAK. Reducing the width of the two annuli resulted in a decrease in both the tractions transmitted to the gel and internal radial stress, however, even when the adhesion percentage was reduced by 61% (from 36% of the disk with $r_1 = 0.8$ to 14% with $r_t = 0.04$), the reduction in total traction and internal stress was stil only 4%. We further considered a non-uniform pattern of adhered spots distributed between the two annuli with $r_t = 0.06$ (Fig. 4D), where spots had radius $r_s = 0.0167$; the spots were selected from the same square grid that was used in Fig. 4A to fill the desired domain. This addition of adhesions between the two annuli results in traction and stress values that lie between the cases of completely adhered annulus and two annuli without spots, as expected. Finally, we include a selection of spots randomly selected from a square grid with 40 squares across the diameter of the internal region as shown in Fig. 3. This addition of internal spots makes only 1% difference to the total traction and internal stress calculated from the model simulations, despite increasing the adhered area from 26% to 37% of the whole surface area of the cell layer.

	Adhesion percentage	T_{total}	T_{total} of $T_{total}(r_1 = 0.8)$	$\sigma_{rr}(r = 0.5)$	$\sigma_{rr}(r = 0.5)$ of $\sigma_{rr}(r = 0.5; r_1 = 0.8)$
RINGS, e.g. Fig. 4B					
$r_1 = 0.7$	51%	4.39	101%	0.72	101%
$r_1 = 0.75$	44%	4.38	100%	0.72	101%
$r_1 = 0.8$	36%	4.37	100%	0.72	100%
$r_1 = 0.85$	28%	4.33	99%	0.71	99%
$r_1 = 0.9$	19%	4.25	97%	0.69	96%
$r_1 = 0.95$	10%	4.01	92%	0.65	90%
$r_1 = 0.975$	5%	3.60	83%	0.58	81%
TWO THIN RINGS, e.g. Fig. 4C					
$r_t = 0.04$	14%	4.18	96%	0.69	96%
$r_t = 0.06$	22%	4.29	98%	0.70	98%
$r_t = 0.08$	29%	4.34	99%	0.71	99%
TWO THIN RINGS WITH SPOTS					
Fig. 4D	26%	4.31	99%	0.71	99%
Fig. 3	37%	4.35	100%	0.72	100%
Fig. 4E	62%	4.36	100%	0.72	101%

Table 2: Sensitivity analysis of different adhesion simulations of annular adhesion patterned gel with contractility maintained at $P_0 = 1$. Total traction, T_{total}, and radial stress at point of ablation, $\sigma_{rr}(r = 0.5)$, are computed for different adhesion patterns (shown in Fig. 4) on a gel with stiffness $\gamma = 15$. The values are also given relative to an annulus with internal radius $r_1 = 0.8$ simulating perfect adhesion across the micropattern. Adhesion percentage denotes the proportion of the circular geometry that is 'adhered'.

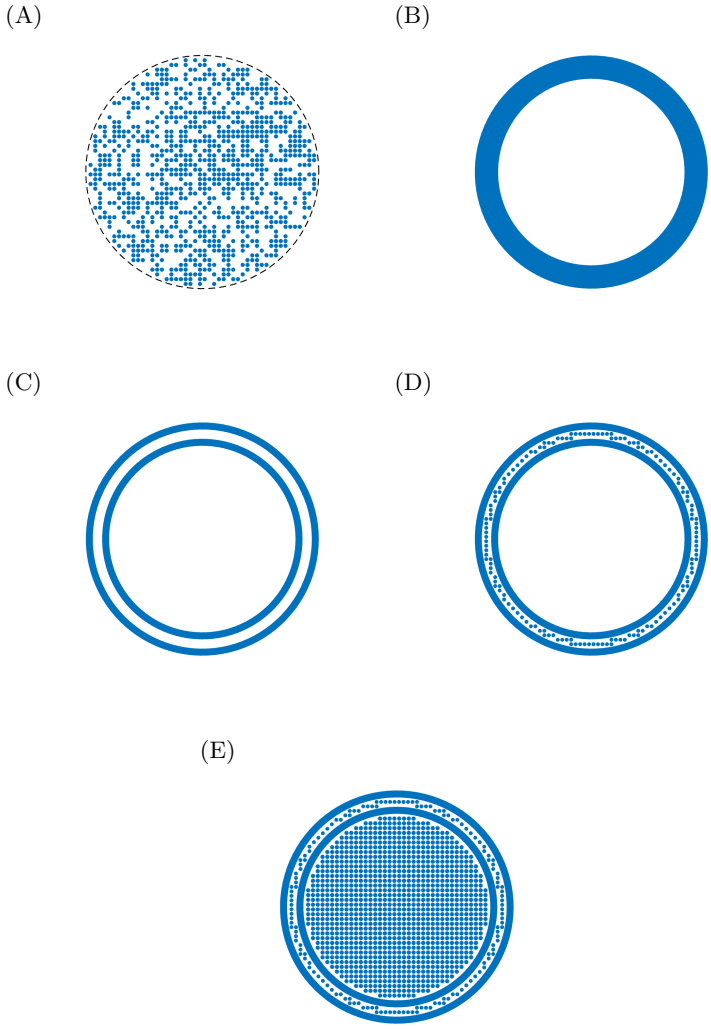

Figure 4: Computational adhesive patterns used for sensitivity analysis: (A) shows a distribution of 935 adhesive spots randomly selected from a uniform grid across a circular geometry for an adhesion coverage of 30%; (B) shows adhesion across an annular region. The internal radius of the annulus is $r_1 \times r_0$, where r_0 is the external radius; here $r_1 = 0.8$ is depicted; (C) shows adhesion across two annuli for a circular geometry. Both annuli have width $r_t \times r_0$, here the inner-most radius is $r_1 = 0.8$ and $r_t = 0.06$; (D) shows adhesion across the same geometry as (C) with additional adhesive spots between the two annuli. These spots have radius $r_s = 0.017$; (E) shows adhesion across the same geometry as (D) with additional adhesive spots in a square grid with 40 grid squares across the diameter of the internal region. These spots have radius $r_s = 0.018$.

Solving for deformations

Analytical solutions for complete adhesion on disk and ring

For an adhered disk, $T(\mathbf{x}) \equiv 1$ across $|\mathbf{r}| < r_0$ analytical solutions of (2) can be obtained with both $P = P_0$ and $P(r) = a(1 + br^5)$, see [4]. In both cases, symmetry implies the deformations will be purely radial so that $\mathbf{u} = u(r)\mathbf{e_r}$. For $P = P_0$,

$$\frac{u}{r_0} = \frac{-P_0(1+\nu)}{2\left(\gamma I_0(\gamma) - (1-\nu)I_1(\gamma)\right)} I_1\left(\frac{\gamma r}{r_0}\right), \tag{3}$$

where I_1 is the modified Bessel function and $\gamma^2 = K(1-\nu^2)r_0^2/hE$. For the radially varying profile we obtain

$$\frac{u(r/r_0)}{r_0} = \frac{(1+\nu)}{2\gamma}\left(cI_1\left(\frac{\gamma r}{r_0}\right) + \frac{5ab}{\gamma^5}\left[\gamma^4 r^4 + 15\gamma^2 r^2 - \frac{45\pi}{2}L_1\left(\frac{\gamma r}{r_0}\right)\right]\right), \tag{4}$$

where we have defined

$$c := \frac{-a(1+b)}{F(\gamma)} + \frac{5ab}{\gamma^5 F(\gamma)}\left[(1-\nu)\left(\gamma^3 + 15\gamma - \frac{45\pi}{2\gamma}L_1(\gamma)\right) - \left(5\gamma^3 + 45\gamma - \frac{45\pi}{2}L_0(\gamma)\right)\right],$$

given in terms of the modified Struve functions $L_0(z)$ and $L_1(z)$ [9]. Note we use non-dimensional scaled spatial variables here (i.e. introducing r/r_0) to enable solutions to be domain size independent, in this formulation b is now also scaled to be non-dimensional so that $b = b^*/r_0^5$ (where $b^* \equiv b$ in dimensional variables). Function $F(\gamma)$ is defined by

$$F(z) := I_0(z) + \frac{(\nu-1)}{z}I_1(z).$$

Similarly analytical solutions for both contractility profiles ($P = P_0$ and $P(r) = a(1 + br^5)$) can be obtained for the adhered ring pattern, provided symmetry is maintained and no distributed adhesions spots are assumed. However, in this case the solutions are more mathematically complicated involving additional special functions. See [4] for the full details of these solutions and their derivations. We note that the parameter $\gamma^2 = K(1-\nu^2)r_0^2/hE$ continues to be the control parameter in the analytical solutions.

Numerical solutions for pFAK informed adhesion patterns

When considering adhesions distributed in discrete regions, such as the adhesion geometry shown in Fig. 3, numerical solutions must be obtained using finite element methods. We again work on the non-dimensional domain scaled to have maximum radius 1, as such we continue to interpret parameter b in the non-dimensional sense as for the analytic solutions. For each defined geometry, a mesh was generated automatically using the generateMesh command within the MATLAB PDE Toolbox (with `Hmax`, maximum edge length, set at 0.005). The force balance equation may be expressed as a general elliptic PDE in two dimensions

$$\begin{aligned} -\nabla\cdot(c_{11}\nabla u_1) - \nabla\cdot(c_{12}\nabla u_2) + a_{11}u_1 + a_{12}u_2 &= f_1 \\ -\nabla\cdot(c_{21}\nabla u_1) - \nabla\cdot(c_{22}\nabla u_2) + a_{21}u_1 + a_{22}u_2 &= f_2. \end{aligned}$$

As in the radially symmetric cases of a complete adhesion or an adhered ring, we have normalised length scales by the cell radius r_0. Thus, specifically the coefficient matrices are

$$c_{11} = \begin{pmatrix} 1 & 0 \\ 0 & \frac{(1-\nu)}{2} \end{pmatrix}, \quad c_{12} = \begin{pmatrix} 0 & \nu \\ \frac{(1-\nu)}{2} & 0 \end{pmatrix}, \quad c_{21} = \begin{pmatrix} 0 & \frac{(1-\nu)}{2} \\ \nu & 0 \end{pmatrix}, \quad c_{22} = \begin{pmatrix} \frac{(1-\nu)}{2} & 0 \\ 0 & 1 \end{pmatrix},$$

$(a_{11}, a_{22}) = T(\mathbf{x})\gamma^2$, and $a_{12} = a_{21} = 0$. With differential contractility given by $P(r) = a(1 + br^5)$, the coefficients on the right-hand-side are given by $f_1 = 5((1+\nu)/2)abx\left(x^2+y^2\right)^{3/2}$ and $f_2 = 5((1+\nu)/2)aby\left(x^2+y^2\right)^{3/2}$, where we have used $r = \left(x^2+y^2\right)^{1/2}$ to convert between Cartesian and polar coordinates. The no stress boundary condition is input as generalised Neumann boundary conditions

$$\begin{aligned} \mathbf{n}\cdot(c_{11}\nabla u_1) + \mathbf{n}\cdot(c_{12}\nabla u_2) + q_{11}u_1 + q_{12}u_2 &= g_1 \\ \mathbf{n}\cdot(c_{21}\nabla u_1) + \mathbf{n}\cdot(c_{22}\nabla u_2) + q_{21}u_1 + q_{22}u_2 &= g_2, \end{aligned}$$

with $\mathbf{n}$ the normal vector to the boundary; $q_{11} = q_{12} = q_{21} = q_{22} = 0$ and $(g_1, g_2) = -((1+\nu)/2)a\left(1 + b(x^2+y^2)^{5/2}\right)\mathbf{n}$. To obtain solutions for a uniform contractility throughout the epithelium, we set $a = P_0$ and $b = 0$.

Parameter fitting to experimental total traction data

From the previous section, we can see that for a given adhesion geometry the model is completely parameterised by γ and ν with either P_0 defined (uniform contractility) or a and b defined (radially varying contractility). The parameters γ and ν are determined from the mechanical properties of the gel and epithelium as described above. The Poisson's ratio for all cells is expected to be close to 0.5 (the value for an incompressible material) and little variation is expected, the specific value 0.45 is taken within the range commonly reported for cells (see table 1).

We used the measured total traction data from the traction force microscopy to set the contractility parameter P_0 or a (for a given choice of b) for each gel stiffness. Specifically for each contractility model (uniform or varying) the model deformations $\mathbf{u}$ are derived as described above and from these deformations the total applied tractions T_{tot} are calculated

$$T_{tot}(P(\mathbf{x})) = \int_A KT(\mathbf{x})\mathbf{u}dA. \tag{5}$$

T_{tot} is then fit to the experimental data of ΣT via $T_{tot} = \Sigma T \cdot A_{pix}$, where A_{pix} is the area of a pixel (here $0.519\mu\text{m}\times0.519\mu\text{m}$).

As an alternative to fitting to the traction data we could have chosen to fit to the total strain energy data. However, as the strain energy data is a derived quantity from the traction force data we chose to fit our single fit parameter to the traction directly. The model with these contractility parameters then subsequently predicts qualitatively similar trends in the strain energy as observed (see e.g. Figs. 4(g,l)), however, on rings, at a slightly higher level than observed. One contributory factor to the observed difference in strain energy is the approximation of a linear spring resistance in the force balance (2), which on finite depth gels and at low adhesion percentages may overpredict strain energy due to the contribution of non-local effects.

When fitting the model with differential contractility, the localisation of contractility to the edge of the layer, b, also needs to be assigned. In the paper, we illustrate the model predictions for a particular choice of parameter values. Namely, we set values of $b = 2.1$ and $b = 0.1$ on the softest

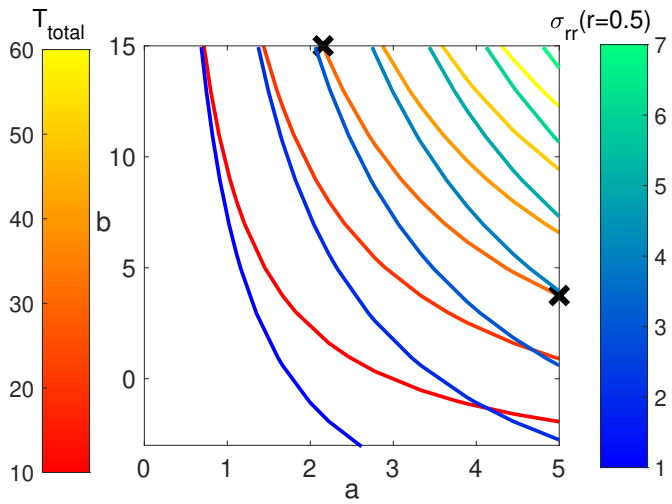

Figure 5: Contour plot shows lines of constant total traction (red-orange) and constant internal stress (blue-green) as a and b are varied. Black crosses mark two choices of a and b parameters such that T_{total} is the same at both points, however, the value of internal stress ($\sigma_{rr}(r = 0.5)$ is different at each point). Here substrate stiffness is kept fixed at $\gamma = 5$.

gels for disk and ring adhesion patterns, respectively. From these initial parameters, we set b values on stiffer gels such that the internal radial stress follows the same trend as the recoil velocity when normalised by their values on the softest gels. Of course, different parametrisations of b could be chosen to reproduce the same qualitative trends. We illustrate this in Fig. 5 where we plot contour lines of constant total traction: this indicates the combination of a and b parameters required to produce a particular value for the total traction for an idealised annular adhesion geometry (e.g. Fig. 4B) on a given stiffness substrate. We further include contours of constant internal stress. As the contours of internal stress and total traction intersect, different parameter choices of b can be used to both fit the experimental total traction data and reproduce the qualitative trends in internal stress. For example, we have indicated two parameter choices with black crosses which correspond to the same total traction but different values of the internal stress.

In the main paper, Figures 4a and b, we show parameter sweeps of contractility scaling parameter a for different stiffness gels with uniform contractility ($b = 0$) *vs* differential contractility ($b = 1$). Fig. 6 demonstrates that the contour lines of constant total traction and internal radial stress depicted in the main paper show general trends in the model, and are not the only suitable values that could have been selected.

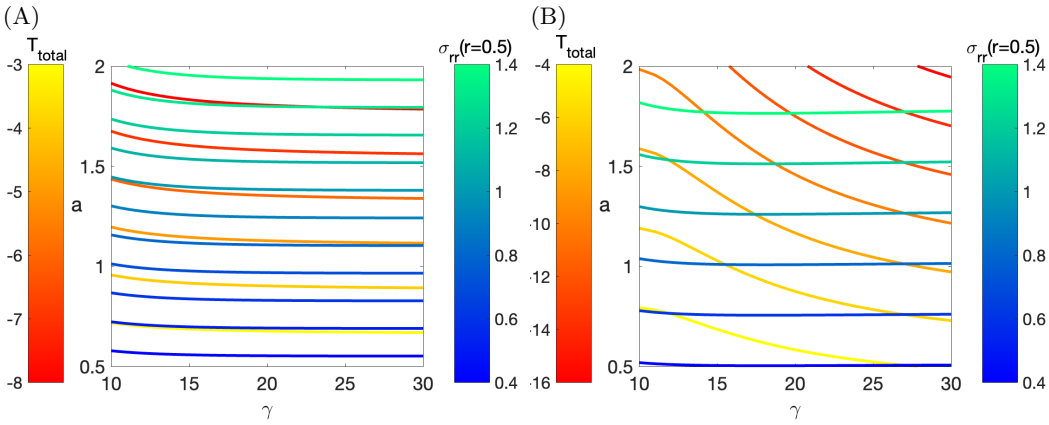

Figure 6: Contour plot shows lines of constant total traction (red-orange) and constant internal radial stress (blue-green) as a is varied on different stiffness substrates. (A) Contractility is uniform ($b = 0$): here the traction and stress contours follow similar trajectories. (B) Contractility is localised to the edge of the layer ($b = 1$): here there is a much greater overlap in traction and stress contour lines.

References

[1] Josephine Solowiej-Wedderburn and Carina. M. Dunlop. Sticking around: Cell adhesion patterning for energy minimization and substrate mechanosensing. *Biophys J*, 121(9):1777–1786, 2022.

[2] Shiladitya Banerjee and M. Cristina Marchetti. Contractile stresses in cohesive cell layers on finite-thickness substrates. *Phys. Rev. Lett.*, 109(10):108101, 2012.

[3] Carina Dunlop. Differential cellular contractility as a mechanism for stiffness sensing. *New Journal of Physics*, 21(6):063005, 2019.

[4] Josephine Solowiej-Wedderburn and Carina M Dunlop. Cell-strain-energy costs of active control of contractility. *Physical review E*, 107(6):L062401, 2023.

[5] F. Mertz, Aaron, S. Benerjee, Yonglu Che, Guy K. German, Ye Xu, Callen Hyland, M. Cristina Marchetti, Valerie Horsley, and Eric. R. Dufresne. Scaling of traction forces with the size of cohesive colonies. *Phys. Rev. Lett.*, 108(19):198101, 2012.

[6] Jordi Alcaraz, Ren Xu, Hidetoshi Mori, Celeste M Nelson, Rana Mroue, Virginia A Spencer, Doug Brownfield, Derek C Radisky, Carlos Bustamante, and Mina J Bissell. Laminin and biomimetic extracellular elasticity enhance functional differentiation in mammary epithelia. *The EMBO journal*, 27(21):2829–2838, 2008.

[7] J Rheinlaender, A Dimitracopoulos, B Wallmeyer, N M Kronenberg, K J Chalut, M C Gather, T Betz, G Charras, and K Franze. Cortical cell stiffness is independent of substrate mechanics. *Nat Mater*, 19(9):1019–1025, 2020.

[8] CA Mullen, TJ Vaughan, MC Voisin, MA Brennan, P Layrolle, and LM McNamara. Cell morphology and focal adhesion location alters internal cell stress. *J R Soc Interface*, 11(101):20140885, 2014.

[9] M Abramowitz and I A Stegun. *Handbook of mathematical functions: with formulas, graphs, and mathematical tables*, volume 55. Courier Corporation, 1964.

Table 1: Main figures statistical values

Figure	N numbers (gels)					Unit	Mean					Standard Deviation					Kruskal-Wallis	Mann-Whitney			
	10	15	20	25	30		10	15	20	25	30	10	15	20	25	30		15	20	25	30
1i	20 (5)	23 (6)	30 (8)	25 (5)	20 (4)	N	122.5	109.6	150.9	104.4	116.7	23.1	23.3	50.9	34.0	26.8	0.006	0.113	0.122	0.098	0.394
1j	28 (11)	29 (11)	23 (7)	23 (6)	28 (7)	N	126.5	109.2	122.1	129.5	137.2	31.2	20.9	34.5	33.2	42.6	0.048	0.049	0.454	0.747	0.476
2c	20 (5)	23 (6)	30 (8)	25 (5)	20 (4)	µm	4.08	2.47	1.18	1.01	0.67	1.95	2.02	0.87	0.51	0.58	1.4×10^{-18}	8.1×10^{-4}	1.3×10^{-7}	3.5×10^{-8}	2.2×10^{-7}
2d	28 (11)	29 (11)	23 (7)	23 (6)	28 (7)	µm	3.34	2.20	2.14	1.11	1.15	2.58	0.97	2.54	0.94	0.80	1.4×10^{-10}	0.123	0.003	1.9×10^{-6}	6.5×10^{-7}
2e	20 (5)	23 (6)	30 (8)	25 (5)	20 (4)	Pa	8.44×10^{7}	4.82×10^{7}	3.51×10^{7}	4.56×10^{7}	2.69×10^{7}	4.35×10^{7}	1.56×10^{7}	2.00×10^{7}	2.22×10^{7}	1.07×10^{7}	4.8×10^{-9}	0.002	2.2×10^{-5}	0.001	2.0×10^{-6}
2f	28 (11)	29 (11)	23 (7)	23 (6)	28 (7)	Pa	5.75×10^{7}	5.13×10^{7}	5.23×10^{7}	4.78×10^{7}	5.91×10^{7}	5.23×10^{7}	2.25×10^{7}	3.15×10^{7}	3.15×10^{7}	2.77×10^{7}	0.255	0.434	0.684	0.421	0.070
2g	20 (5)	23 (6)	30 (8)	25 (5)	20 (4)	Pa	1859.0	1655.1	894.1	1170.6	706.5	824.9	1171.9	645.3	853.0	541.7	3.0×10^{-8}	0.116	3.9×10^{-5}	0.001	2.7×10^{-6}
2h	28 (11)	29 (11)	23 (7)	23 (6)	28 (7)	Pa	1765.8	1630.1	1927.6	1210.7	1724.3	1491.2	1037.3	2326.7	1100.3	1694.7	0.137	0.842	0.201	0.044	0.787
2i	20 (5)	23 (6)	30 (8)	25 (5)	20 (4)	pJ	26399.7	8261.6	3126.2	3272.1	1157.6	24238.5	7927.5	3417.4	3089.4	1355.2	3.2×10^{-14}	0.004	1.6×10^{-6}	3.3×10^{-6}	3.0×10^{-7}
2j	28 (11)	29 (11)	23 (7)	23 (6)	28 (7)	pJ	19440.6	7893.4	9135.1	4291.8	5959.2	42344.8	6744.3	13299.0	5777.0	7889.4	0.001	0.660	0.057	9.6×10^{-4}	0.005
3k	20 (5)	23 (6)	30 (8)	25 (5)	20 (4)	µm/s	0.138	0.136	0.110	0.112	0.110	0.079	0.062	0.050	0.021	0.024	0.172	0.827	0.163	0.758	0.570
3l	28 (11)	29 (11)	23 (7)	23 (6)	28 (7)	µm/s	0.189	0.145	0.131	0.110	0.117	0.083	0.048	0.048	0.051	0.036	6.8×10^{-6}	0.037	0.004	5.5×10^{-5}	2.2×10^{-4}
3o	20 (5)	23 (6)	30 (8)	25 (5)	20 (4)	Pa	-1.79×10^{7}	-1.18×10^{7}	-0.67×10^{7}	-0.75×10^{7}	-0.39×10^{7}	1.46×10^{7}	0.81×10^{7}	0.83×10^{7}	0.42×10^{7}	0.27×10^{7}	1.8×10^{-5}	0.192	0.006	0.023	0.003
3p	28 (11)	29 (11)	23 (7)	23 (6)	28 (7)	Pa	-2.29×10^{7}	-1.27×10^{7}	-1.66×10^{7}	-0.98×10^{7}	-1.30×10^{7}	2.84×10^{7}	0.87×10^{7}	1.52×10^{7}	0.97×10^{7}	1.10×10^{7}	0.068	0.105	0.158	0.007	0.100
3q	20 (5)	23 (6)	30 (8)	25 (5)	20 (4)	pJ	10716.3	3348.6	1435.4	973.7	-323.8	11383.4	5373.9	2772.3	726.9	2680.0	3.4×10^{-10}	0.021	2.3×10^{-4}	5.9×10^{-4}	1.0×10^{-4}
3r	28 (11)	29 (11)	23 (7)	23 (6)	28 (7)	pJ	14753.8	3660.9	3296.1	1548.7	2969.1	29915.0	4381.3	6933.5	2206.8	5415.6	3.4×10^{-5}	0.045	0.008	4.5×10^{-5}	9.3×10^{-5}
5b	32 (3)	22 (3)	69 (3)	48 (3)	61 (3)	16-bit Grey levels	15173.1	15866.3	23751.7	10.974.1	12973.7	7123.3	9272.0	10696.3	5461.2	7753.0	7.9×10^{-15}	0.867	7.1×10^{5}	0.005	0.059
5c	34 (4)	55 (4)	59 (3)	62 (2)	41 (2)	16-bit Grey levels	15836.4	15285.4	16551.1	15368.4	14684.5	8430.0	8312.1	6529.4	7101.4	10850	0.037	0.602	0.980	0.400	0.104
5d	32 (3)	22 (3)	69 (3)	48 (3)	61 (3)	16-bit Grey levels	11168.0	11032.1	16890.4	11593.0	8938.0	5933.1	5240.4	5279.6	5762.0	4645.5	3.4×10^{-19}	0.979	2.1×10^{-7}	0.520	0.008

5e	24 (3)	32 (3)	59 (3)	62 (2)	41 (2)	16-bit Grey levels	16196.4	12414.3	8869.2	12372.9	9840.0	10533.9	6074.4	2161.9	3565.3	4245.2	5.0×10^{-12}	0.048	1.0×10^{-6}	0.081	1.9×10^{-4}
5f	32 (3)	22 (3)	69 (3)	48 (3)	61 (3)	16-bit Grey levels	15750.0	16459.8	15743.4	10402.9	11641.1	3847.4	5954.3	3990.1	3870.0	2873.5	5.4×10^{-17}	0.965	0.899	5.1×10^{-7}	1.1×10^{-6}
5g	34 (4)	55 (4)	59 (3)	62 (2)	41 (2)	16-bit Grey levels	28160.5	35148.9	18770.7	14541.5	17514.6	16042.0	12749.0	6013.8	3282.0	5099.7	7.2×10^{-26}	0.011	0.020	3.1×10^{-6}	0.002
5l (disk)	48 (4)	79 (3)	95 (3)	51 (2)	58 (3)	ratio	1.134	1.028	1.068	1.050	1.043	0.118	0.130	0.130	0.104	0.098	0.003	0.001	0.062	0.003	0.004
5l (ring)	97 (2)	24 (3)	49 (3)	33 (2)	14 (3)	ratio	1.025	1.064	1.034	1.090	1.185	0.079	0.166	0.103	0.218	0.129	2.5×10^{4}	0.505	0.140	8.0×10^{-4}	1.2×10^{-4}

Table 2: Extended data figures statistical values

Figure	N numbers (gels)					Unit	Mean					Standard Deviation					Kruskal-Wallis	Mann-Whitney			
	10	15	20	25	30		10	15	20	25	30	10	15	20	25	30		15	20	25	30
1c	28 (7)	28 (7)	28 (7)	28 (7)	24 (6)	Pa	10810.4	14667.5	19201.8	25494.1	31418.5	2563.2	1574.4	2696.9	3795.2	2794.8	1.2×10^{-60}	1.9×10^{-7}	2.7×10^{-10}	1.3×10^{-10}	6.5×10^{-10}
1d	87 (3)	56 (3)	33 (3)	40 (1)	17 (2)	%	24.0	23.2	21.2	19.6	20.0	3.5	2.3	2.1	2.1	3.0	3.3×10^{-23}	0.002	3.0×10^{-8}	3.4×10^{-13}	1.7×10^{-6}
1e	41 (3)	13 (3)	36 (3)	15 (2)	41 (3)	%	17.6	17.2	14.7	15.4	15.5	1.7	1.7	2.3	1.6	2.5	1.2×10^{-9}	0.342	1.3×10^{-8}	1.5×10^{-4}	7.8×10^{-5}
1j	20 (5)	23 (6)	30 (8)	25 (5)	20 (4)	%	0.32	0.22	0.11	-0.13	0.53	0.90	0.71	1.01	0.71	1.29	0.227	0.970	0.945	0.123	0.560
1k	28 (11)	29 (11)	23 (7)	23 (6)	28 (7)	%	0.47	0.16	-0.42	1.12	0.12	1.62	0.60	1.22	6.72	0.71	0.288	0.615	0.074	0.389	0.652
2g	20 (5)	23 (6)	30 (8)	25 (5)	20 (4)	pixels	542025	218209	121461	114767	61743	307498	84989	67864	46357	24890	1.3×10^{-21}	2.0×10^{4}	4.7×10^{-7}	5.3×10^{-7}	1.2×10^{-7}
2h	28 (11)	29 (11)	23 (7)	23 (6)	28 (7)	pixels	350437	215146	191101	124234	122272	324791	87074	125988	84106	55581	1.2×10^{-11}	0.031	0.003	$2.8 \times 10^{-}$	6.7×10^{-8}
3i	20 (5)	23 (6)	30 (8)	25 (5)	20 (4)	seconds	26.2	16.9	20.6	18.6	22.2	295.3	81.2	45.7	36.5	111.7	0.705	0.336	0.317	0.174	0.457
3j	28 (11)	29 (11)	23 (7)	23 (6)	28 (7)	seconds	24.2	18.9	21.6	20.1	19.2	40.7	157.5	410.8	744.7	49.4	0.961	0.955	0.656	0.932	0.550